This is the submitted version of the following article:

Serrà A., Zhang Y., Sepúlveda B., Gómez E., Nogués J., Michler J., Philippe L.. Highly reduced ecotoxicity of ZnO-based micro/nanostructures on aquatic biota: Influence of architecture, chemical composition, fixation, and photocatalytic efficiency. Water Research, (2020). 169. 115210: - . 10.1016/j.watres.2019.115210,

which has been published in final form at https://dx.doi.org/10.1016/j.watres.2019.115210 © https://dx.doi.org/10.1016/j.watres.2019.115210. This manuscript version is made available under the CC-BY-NC-ND 4.0 license http://creativecommons.org/licenses/by-nc-nd/4.0/

Highly reduced ecotoxicity of ZnO-based micro/nanostructures on aquatic biota: Influence of architecture, chemical composition, fixation, and photocatalytic efficiency

Albert Serrà [l,*], Yue Zhang [&], Borja Sepúlveda [&], Elvira Gómez [$, @], Josep Nogués [&, #], Johann Michler [l], Laetitia Philippe [l]

[l] Empa, Swiss Federal Laboratories for Materials Science and Technology, Laboratory for Mechanics of Materials and Nanostructures, Feuerwerkerstrasse 39, CH-3602 Thun, Switzerland.

[&] Catalan Institute of Nanoscience and Nanotechnology (ICN2), CSIC and BIST, Campus UAB, Bellaterra, E-08193 Barcelona, Spain.

[$] Grup d'Electrodeposició de Capes Primes i Nanoestructures (GE-CPN), Departament de Ciència de Materials i Química Física, Universitat de Barcelona, Martí i Franquès, 1, E-08028, Barcelona, Catalonia, Spain.

[@] Institute of Nanoscience and Nanotechnology (IN^{2}UB), Universitat de Barcelona, Barcelona, Catalonia, Spain.

[#] ICREA, Pg. Lluís Companys 23, E-08010, Barcelona, Spain.

Corresponding author: albert.serraramos@empa.ch (A.S.)

ABSTRACT

Developing efficient sunlight photocatalysts with enhanced photocorrosion resistance and minimal ecotoxicological effects on aquatic biota is critical to combat water contamination. Here, the role of chemical composition, architecture, and fixation on the ecotoxicological effects on microalgae of different ZnO and ZnO@ZnS based water decontamination photocatalysts was analyzed in depth. In particular, the ecotoxicological effects of films, nanoparticles and biomimetic micro/nano-ferns were carefully

assessed by correlating the algae's viability to the Zn(II) release, the photocatalyst–microalgae interaction, and the production of reactive oxygen species (ROS). The results showed a drastic improvement in algal viability for supported ZnO@ZnS core@shell micro/nanoferns, as their ecotoxicity after 96 h light exposure was significantly lower (3.7–10.0% viability loss) compared to the ZnO films (18.4–35.5% loss), ZnO micro/nanoferns (28.5-53.5% loss), ZnO nanoparticles (48.3–91.7% loss) or ZnO@ZnS nanoparticles (8.6-19.2% loss) for catalysts concentrations ranging from 25 mg L^{-1} to 400 mg L^{-1}. In particular, the ZnO@ZnS micro/nanoferns with a concentration of 400 mg L^{-1} exhibited excellent photocatalytic efficiency to mineralize a multi-pollutant solution (81.4±0.3% mineralization efficiency after 210 min under UV-filtered visible light irradiation) and minimal photocorrosion (< 5% of photocatalyst dissolution after 96 h of UV-filtered visible light irradiation). Remarkably, the ZnO@ZnS micro/nanoferns showed lower loss of algal viability (9.8±1.1%) after 96 h of light exposure, with minimal reduction in microalgal biomass (9.1±1.0%), as well as in the quantity of chlorophyll-a (9.5±1.0%), carotenoids (8.6±0.9%) and phycocyanin (5.6±0.6%). Altogether, the optimized ZnO@ZnS core@shell micro/nanoferns represent excellent ecofriendly photocatalysts for water remediation in complex media, as they combine enhanced sunlight remediation efficiency, minimal adverse effects on biological microorganisms, high reusability and easy recyclability.

GRAPHICAL ABSTRACT

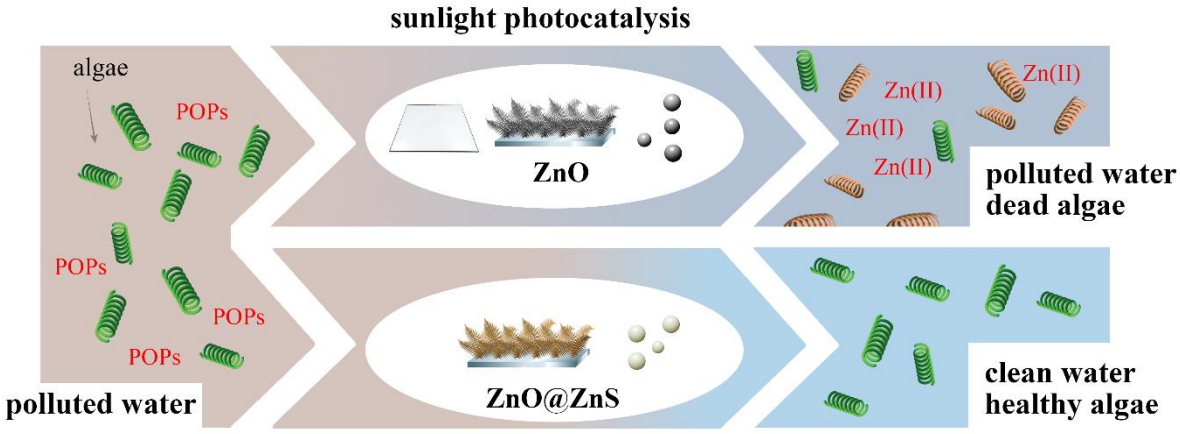

KEYWORDS: ecotoxicity, ZnO-based photocatalysts, sunlight photocatalysis, microalgae, persistent organic pollutants

1. INTRODUCTION

The decontamination of wastewater is one of the main challenges of this century since high levels of pollution resulting from anthropological and industrial activities have important negative effects on ecosystems and on human life and health (Fu et al., 2011; McMullan et al., 2011; Gleik, 1993; Jury, 2007). Currently, the main processes for the decontamination of wastewater are largely ineffective for the elimination of many pollutants, especially persistent organic pollutants (POPs) (Chong, et al., 2010; Malato, et al., 2009; Moreira, et al., 2017, Serrà, et al., 2019). POPs include pesticides, drugs, hormones, personal hygiene products, etc. Given the severe negative effects of POPs on biota, their efficient elimination is critical. In phytoplankton communities in particular, many POPs can directly or indirectly facilitate the growth of microorganisms—for example, by stimulating cyanobacterial blooms—and consequently modify population growth (Harris, et al., 2016; Everaert, et al., 2015; Bettinetti, et al., 2012; Maule, et al., 1984).

In this context, photocatalysis offers an excellent decontamination strategy by exploiting the solar energy for the total remediation of POPs to provide a clean, green, and sustainable approach (Lee, et al., 2016; Batista, et al., 2017). This is motivating the rapid proliferation of new efficient photocatalysts, especially semiconducting materials such as TiO_2 or ZnO, that enable rapid water decontamination. Many of these photocatalysts are also effective as antifungal and antibacterial multitasking platforms (Liu, et al., 2018; Hatamie, et al., 2015). Current photocatalyst design is focused on developing new materials, architectures, and configurations to improve their mineralization efficiency, especially under sunlight irradiation. Researchers have also invested significant effort into identifying and understanding the remediation mechanisms, including the production of reactive species and different intermediates (Serrà, et al., 2019; Liu, et al., 2018; Hatamie, et al., 2015, Yadav, et al., 2016; Arshad, et al. 2017). However, researchers have rarely analyzed the potentially disastrous side effects of photocatalysts, especially for aquatic microorganisms. Therefore, it is crucial to develop materials that affect minimally the biota throughout their whole life cycle by considering all the potential impacts on the ecosystems in which they will be used.

In the particular case of ZnO photocatalysts, their extensive use in a wide variety of industrial applications and consumer products increases the risk of release into aquatic environments, where they can cause ecotoxicological effects (Mortimer, et al, 2010; Djeramane, et al. 2018; Subashchandrabose, et al. 2013). The toxicity can be especially relevant for some microorganisms, such as microalgae, which play a fundamental role in the ecosystem as primary food sources for aquatic biota (Singh, et al., 2017; Mani, et al., 2014; Khan, et al., 2011). Therefore, although ZnO photocatalysts could seem a clean and economical method for water decontamination, they can also have adverse effects on ecosystems and human life. The main route of ZnO contamination is the release and accumulation of the micro- and nano-ZnO structures in aquatic environments, and the subsequent liberation of Zn(II) caused by the extremely high ZnO photocorrosion (Mortimer, et al, 2010; Djeramane, et al. 2018; Subashchandrabose, et al. 2013).

However, in the particular case of microalgae, the ZnO damage could be more complex and involve the following factors: (i) physical or mechanical damage because of the direct contact of micro- and nanomaterials with the fragile microalgae; (ii) the high level of dissolved Zn(II) in the aquatic media due to the high capability of algae to adsorb metal ions, and (iii) the generation of reactive oxygen species (ROS) during exposure of ZnO to sunlight. Moreover, diverse factors, such as shape, porosity, size, surface coating, exposure mode and time, have determinant effects on the ecotoxicology of these photocatalysts in aquatic microorganisms (Bondarenko, et al., 2013; Hou, et al., 2018; Aruoja, et al., 2009; Ma, et al., 2013; Miao, et al., 2010; Wong, et al., 2010). Consequently, there is an urgent need to find and thoroughly analyze different photocatalytic ZnO architectures which could combine excellent pollutant degradation efficiency and minimal ecotoxicity on algae.

In this work, we present a comprehensive ecotoxicological and photocatalytic analysis of different ZnO and ZnO@ZnS core@shell micro/nanostructures as a way to highlight the importance of integrating ecotoxicity and photocatalysis efficiency in the water decontamination process, by considering the whole life cycle of the photocatalyst. To analyze the effect of the photocatalyst architecture on microalgae ecotoxicity, three different systems were evaluated: (i) ZnO films, which are characterized by a continuous supported/fixed structure with low active surface area, minimal direct interaction/contact with aquatic microorganisms, low photocatalytic activity, and low ROS production efficiency under

sunlight irradiation; (ii) supported/fixed ZnO fern-like microstructured arrays, showing high active surface areas due to their fractal architecture, which potentially increases the direct interaction with aquatic microorganisms, as well as the pollutant adsorption and light trapping capability, thus increasing the photocatalytic and ROS production efficiencies under sunlight irradiation; and (iii) ZnO nanoparticles, being one of the most relevant ZnO residues in many industrial applications and consumer products, which exhibit high surface area, strong direct interaction with aquatic microorganisms, and moderate photocatalytic and ROS production efficiencies under sunlight irradiation. Additionally, the effect of the chemical composition was also analyzed by comparing ZnO and ZnO@ZnS core@shell photocatalysts. This analysis is motivated by the recent demonstration of the improved photocatalytic performance provided by the ZnS shell due to the increased ROS production under sunlight irradiation while significantly reducing the photocorrosion activity (Serrà, et al., 2019; Ranjith, et al., 2018). Importantly, here we demonstrate that optimized ZnO@ZnS core@shell fern-like biomimetic microleaf arrays supported on solid substrates can efficiently combine low ecotoxicological effects with highly enhanced photocatalytic efficiency compared to other ZnO and ZnO@ZnS core@shell micro- and nanostructures. To demonstrate these features, we have investigated the photocorrosion resistance, and the dose- and time-dependent toxicity of these nanostructures with different architectures in *Spirulina (Arthrospira) platensis* (microalgae), to specifically determine the relationship between the ecotoxicological effects and the photocatalyst size, shape, composition, configuration (dispersed vs. supported), and efficiency.

2. EXPERIMENTAL SECTION

2.1. Synthesis of ZnO-based photocatalysts

ZnO films were hydrothermally grown on a glass substrate using solution of 0.01 M hexamethylenetetramine (#398160; Sigma-Aldrich, > 99.0%) and 0.1 M $Zn(NO_3)_2$ (#398160; Sigma-Aldrich, > 99.0%), with the pH was adjusted to 10, for 30 min at 65°C under magnetic stirring conditions (600 rpm) (Vessalli, et al., 2017; Mizuta, et al., 2006).

ZnO fern-like microleaf arrays were potentiostatically electrodeposited at -1.0 V (vs. Ag/AgCl/KCl (3 M)) – 28 C cm^{-2} of circulated charge density – using a conductive fluorine-doped tin oxide film on a

glass substrate with a classical three-electrode electrochemical cell, an Autolab with PGSTAT30 potentiostat/galvanostat (Metrohm Autolab; Netherlands), and the NOVA software (Version 2.1.4; Metrohm Autolab; Netherlands). Working, counter, and reference electrodes were the fluorine-doped tin oxide film on a glass substrate, a Pt mesh, and Ag/AgCl/KCl (3 M), respectively. The electrochemical medium was a 0.5 mM $ZnCl_2$ (#14422; Fluka, > 98.0%) + 0.1 M KCl (#P9333; Sigma-Aldrich, > 99.0%) oxygen-saturated (bubbled 45 min before and during the electrodeposition) aqueous solution (pH = 7 in standard conditions) maintained at 80°C. The electrodeposition process was performed under strong stirring conditions (400 rpm of magnetic stirring and 12 L min^{-1} of oxygen bubbling).

To form ZnO@ZnS core@shell microstructures, the ZnO micro/nanoferns were immersed in an aqueous solution of 30 mM thioacetamide (TAA) – CH_3CSNH_2 – (#163678; Sigma-Aldrich, 98%) at 50°C in a water bath for 4, 8, and 12 h. These structures are denoted as ZnO@ZnS(4h), ZnO@ZnS(8h), and ZnO@ZnS(12h) micro/nanoferns, respectively. The ZnO and ZnO@ZnS core@shell micro/nanofern arrays were then exhaustively washed with water and ethanol, dried at room temperature, and annealed for 2 h at 400°C in an argon atmosphere. The annealing treatment was performed using a rapid thermal annealing equipment (Advance Riko Mila 5050; Japan). The heating ramp rate was set at 10°C min^{-1}.

The ZnO@ZnS nanoparticles were fabricated using commercial 20 nm ZnO nanoparticles (99.5%; IoLiTec Nanomaterials; Germany) as seeds, following the same sulfidation process with thioacetamide for 4 h.

2.2. Characterization of ZnO-based photocatalysts

The surface morphologies and the elemental composition were examined by Hitachi S-4800 and H-4100FE field-emission scanning electron microscopy (FE-SEM; Hitachi; Japan) equipped with energy-dispersive X-ray spectroscopy detector. The ZnO and ZnO/ZnS nanoparticles were analyzed using a high-resolution HR-TEM Jeol JEM 2100 (Jeol; Japan) equipped with a LaB_6 source operated at 200 kV (images were recorded with Digital Micrograph v.1.82.80 software). Nanoparticles were dispersed in ethanol, and then a droplet of the suspension was poured in Holey Carbon covered copper TEM grids (300 Mesh Cu, Agar Scientific; United Kingdom) prior to HR-TEM observation. The particle size

distribution was evaluated by analyzing more than 120 nanoparticles. The specific surface area of each biomimetic photocatalyst was determined by the Brunauer–Emmett–Teller (BET) method from N_2 adsorption-desorption isotherms at 77 K using a Micrometrics Tristar-II (Micrometrics; Canada). The structural characterization was conducted using X-ray diffraction (XRD, Bruker D8 Discover diffractometer; Bruker; United States) in the Bragg–Brentano configuration with CuK_α radiation. The optical and electrical properties of the photocatalysts were analyzed by recording the UV-vis diffused reflectance spectra (DRS) and photoluminescence. DRS were measured using a UV-vis PerkinElmer Lambda 900 UV spectrophotometer (PerkinElmer; United States). The photoluminescence was acquired with a custom-made set-up based on a narrow band filtered (FB360-10; Thorlabs; United States) light emitting diode with central emission at 365 nm (M365FP1; Thorlabs; United States) as excitation source. The back scattered luminescence was long pass filtered (FEL0400; Thorlabs; United States) and detected by an Andor 193i spectrometer with an Andor Idus camera (Andor technology, United Kingdom).

2.3. Photocatalytic efficiency of the ZnO-based photocatalysts

The photocatalytic activity was examined by monitoring the decomposition of a complex solution of three different POPs (5 ppm of methylene blue (MB) (#M9140; Sigma-Aldrich, > 82 %) + 5 ppm of 4-nitrophenol (4-NP) (#73560; Honeywell Fluka, > 99 %) + 5 ppm of Rhodamine B (Rh-B) (#83689; Sigma-Aldrich, > 98 %) pollutants) under a 75 W Xe lamp setup with UV-filtered simulated sunlight (light intensity of 678 ± 11 lx) or natural UV-filtered sunlight (average light intensity 1471 ± 275 lx). Longpass filters (cut-on wavelength region: 400 nm to 2200 nm) were introduced to limit wavelength radiation and to avoid direct photolysis of the pollutants. Pollutant solutions were prepared in algal culture medium. The photocatalysts (400 mg L^1) were immersed first in each pollutant solution in dark conditions for 60 min to reach adsorption-desorption equilibrium before starting the light actuation. The photoremediation process was followed at 30°C and under argon bubbling using the following the comparison of the total organic content (TOC) prior to the start of irradiation and after irradiating the sample for 210 min, by using the high-temperature combustion method on a catalyst ($Pt\text{-}Al_2O_3$) in a tubular flow microreactor operated at 680°C, with a stream of hydrocarbon free air to oxidize the organic carbon, using TOC analyzer (model TOC-V_{CSH}; Shimadzu Corporation; Japan) with a high-sensibility

column. In addition, the ZnO-based photocatalysts were recycled/reused for eight consecutive cycles to mineralize the three multi-pollutant solution under UV-filtered natural sunlight to test their reusability and recyclability properties. Each experiment was repeated four times to ensure accuracy and reproducibility.

2.4. Reactive oxygen species identification

Chemical selective radical quenchers were used to determine the formation of hydroxyl radicals ($^{\bullet}OH$), oxygen superoxide ions (O_2^{-}), and singlet oxygen ($^1O_2$) by the ZnO-based photocatalysts under UV-filtered simulated sunlight (> 400 nm, light intensity of 678 ± 11 lx) at 30°C. The hydroxyl radical ($^{\bullet}OH$) concentration was measured by following the time-dependent reduction of the fluorescence peak at 515 nm (λ_{ex} = 303 nm) in quartz cuvettes containing 8 µM of fluorescein sodium salt (#30181; Supelco/Sigma-Aldrich) using an AMINCO-Bowman Series 2 spectrofluorometer (Thermo Electron; United States). The reaction between 100 µM of XTT [2,3-Bis(2-methoxy-4-nitro-5-sulfophenyl)-2H-tetrazolium-5-carboxanilide] sodium salt (#X4251; Supelco/Sigma-Aldrich, > 90%) and the formed oxygen superoxide ions (O_2^{-}) allowed to identify the formation of oxygen superoxide ions by measuring the characteristic absorption peak of XTT-formazan (resulting from the reduction of XTT by superoxide ions) at 475 nm by using a UV-1800 Shimadzu UV-vis spectrophotometer (Shimadzu Corporation; Japan). The singlet oxygen ($^1O_2$) formation was determined by a highly selective singlet oxygen sensor green (SOSG) reagent (Invitrogen; United States). The formation of singlet oxygen was monitored by measuring the time-dependent photoluminescence intensity at 535 nm (λ_{ex} = 488 nm) using an AMINCO-Bowman Series 2 spectrofluorometer (Thermo Electron; United States), which corresponds to the formation of the endoperoxide SOSG-$^1O_2$ produced by the reaction of the anthracene part of SOSG reagent (5mM in methanol) with the singlet oxygen.

2.5. Photostability and photocorrosion resistance of the ZnO-based photocatalysts

The photostability and photocorrosion activity of the different ZnO-based photocatalysts were evaluated by (i) determining the evolution of the concentration of Zn(II) ions in the algal culture medium, (ii) measuring the BET surface area, and (iii) examining the surface by SEM after the irradiation of each

photocatalyst with UV-filtered simulated sunlight during 96 h (light intensity of 658 ± 25 lx). The algal culture medium consists on: 4.5 g L^{-1} of $NaHCO_3$ (#13433; Fluka, > 99 %), 0.5 g L^{-1} of K_2HPO_4 (#60356; Fluka, > 99 %), 1.5 g L^{-1} of $NaNO_3$ (#S5506; Sigma-Aldrich, > 99 %), 1.0 g L^{-1} of K_2SO_4 (#P0772; Sigma-Aldrich, > 99 %), 1.0 g L^{-1} of NaCl (#S7563; Sigma-Aldrich, > 99.5 %), 1.2 g L^{-1} of $MgSO_4$ (#746452; Sigma-Aldrich, > 99.5 %), and 0.04 g L^{-1} $CaCl_2$ (#793639; Sigma-Aldrich, > 96 %), 0.001 g L^{-1} of $FeSO_4 \cdot 7H_2O$ (#F8263; Sigma-Aldrich, > 99 %) (Wang, et al, 2007; Lone, et al., 2013). The concentration of Zn(II) ions in the algal culture medium was determined by measuring the absorbance at 620 nm, associated to the Zn(II)-Zincon complex, in a quartz cuvette with an optical length of 1 cm using a UV-1800 Shimadzu UV-vis spectrophotometer (Shimadzu Corporation; Japan). Prior to measuring the absorbance, 100 µL of algal culture medium were incubated at 20°C for 10 min with 900 µL of 40 µM Zincon monosodium salt (#96440; Sigma-Aldrich) in borate buffer (50 mM, pH = 9). Metal stock solution of Zn(II) was prepared by dissolving the appropriate amount of $ZnCl_2$ (#14422; Fluka, > 98.0%) in algal culture medium. To evaluate the possible interference of iron ions from the algal medium in the determination of the Zn(II) ions, metal stock solutions of Zn(II) were also prepared in MilliQ water. Note that Fe(III) ions can interfere when they are present in concentrations higher than 5 mg L^{-1}, while Fe(II) does not interfere. Our results indicate that the algae medium did not interfere in the determination of Zn(II) using the Zincon monosodium salt due to the high selectivity for Zn(II) ions and the low concentration of ferric ions (<1 mg L^{-1} in our case).

2.6. Ecotoxicity of the ZnO-based photocatalysts

The microalgae *Spirulina (Arthrospira) platensis* –"*paracas*" type –was cultivated in an algal culture medium (pH 9.8) under a temperature of 30°C, solar illumination, and air bubbling. The bioassays were conducted using ZnO-based photocatalysts at the following concentrations: 0, 25, 50, 100, 200, and 400 mg L^{-1}. Irradiation experiments were performed to analyze the effect of (i) the architecture, (ii) the chemical composition, and (iii) the fixation of photocatalysts on microalgae:

(i) *Architecture effect:* Different concentrations of ZnO films, ZnO nanoparticles, and ZnO micro/nanoferns were immersed in a microalgae culture and irradiated with continuous simulated

sunlight (light intensity of 740 ± 15 lx) for 8 h per day for four days. The microalgae viability, biomass reduction, and photosynthetic pigment reduction were measured after 6, 12, 24, 72, and 96 h.

(ii) *Composition effect:* Different concentrations of ZnO and ZnO@ZnS nanoparticles and micro/nanoferns were immersed in a microalgae culture and irradiated with continuous simulated sunlight (light intensity of 740 ± 15 lx) for 8 h per day for four days. The microalgae viability, biomass reduction, and photosynthetic pigment reduction were measured after 6, 12, 24, 72, and 96 h.

(iii) *Fixation effect:* Different concentrations of fixed and non-fixed ZnO@ZnS micro/nanoferns (sulfidation time of 4 h) were immersed in the microalgae culture and then were irradiated 8 h per day with continuous simulated sunlight (light intensity of 740 ± 15 lx) for 8 h per day for four days. The microalgae viability, biomass reduction, and photosynthetic pigment reduction were measured after 6, 12, 24, 72, and 96 h.

The microalgae survival was estimated as the percentage of viability loss in microalgae with respect to the control (0 mg L^{-1} of photocatalyst). For this purpose, 1 mL of each suspension was loaded in a Sedgewick-Rafter cell (SPI supplies, Graticules S50; Structure Probe Inc, United States) to count the number of microalgae non-distorted in shape or size. The quantification of the biomass reduction was determined by optical density measurements at 560 nm using a UV-1800 Shimadzu UV-vis spectrophotometer (Shimadzu Corporation; Japan) during the incubation period. *Spirulina (arthrospira) platensis* include chlorophyll-a, carotenoid, and phycocyanin photosynthetic pigments. The chlorophyll-a, and carotenoid pigments were measured using the Lichtenthaler and Wellburn method (Deniz, et al., 2011; Khan, et al., 1987; Dere, et al., 1998). During the incubation period, 3 mL of suspensions were taken and centrifuged at 5000 rpm for 10 min. Then the sample was washed with phosphate buffer saline (0.1 M, pH = 7) solution three times. After discarding the supernatant, ethanol (96% v/v) was added to the microalgae residues and thoroughly mixed, and the pigments were extracted in ethanol at 65°C for 90 min. Then, the absorbance of the supernatant in the ethanol solution at 470, 649, and 665 nm was measured using a UV-1800 Shimadzu UV-vis spectrophotometer (Shimadzu Corporation; Japan). The

concentration of chlorophyll-a, and carotenoids was calculated according to Lichtenthaler and Wellburn equations (Deniz, et al., 2011; Khan, et al., 1987; Dere, et al., 1998). For the phycocyanin concentration determination, 0.5 mL of microalgae suspension were taken and centrifuged at 10,000 rpm for 10 min and washed with phosphate buffer saline solution (0.1 M, pH = 7) three times. The pellets were then resuspended in phosphate buffer saline solution (0.1 M, pH = 7) and ultrasonicated for 30 min to break the microalgae filaments. Then, the resultant suspension was centrifuged at 4°C 10,000 rpm for 5 min, and the absorbance of the supernatant solution at 615 and 652 nm was measured using a UV-1800 Shimadzu UV-vis spectrophotometer (Shimadzu Corporation; Japan). The concentration of phycocyanin was calculated according to the Bennett and Bogorad equation (Moraes, et al., 2011; Bennett, et al., 1973).

3. RESULTS AND DISCUSSION

3.1. Synthesis and characterization of the different ZnO-based structures

With the aim to identify the photocatalysts that can combine highly efficient POPs mineralization and minimal toxicity on aquatic biota, we have analyzed in this work the roles of shape, chemical composition, and fixation of different ZnO-based micro/nanoarchitectures (**Figure 1**) on microalgae The effect of the shape has been established by comparing: (i) ZnO films chemically deposited on glass; (ii) ZnO dendritical micro/nanoferns electrodeposited on fluorine-doped tin oxide films on a glass substrate; and (iii) commercial ZnO nanoparticles. The effect of the chemical composition has been assessed by comparing both ZnO and ZnO@ZnS core@shell micro/nanoferns and nanoparticles, which were prepared by chemical sulfidation and thermal annealing (**Figure 2a**). Finally, the effect of fixation has been analyzed by comparing fixed and non-fixed ZnO@ZnS micro/nanoferns (i.e., detached from the fluorine-doped tin oxide film on a glass substrate).

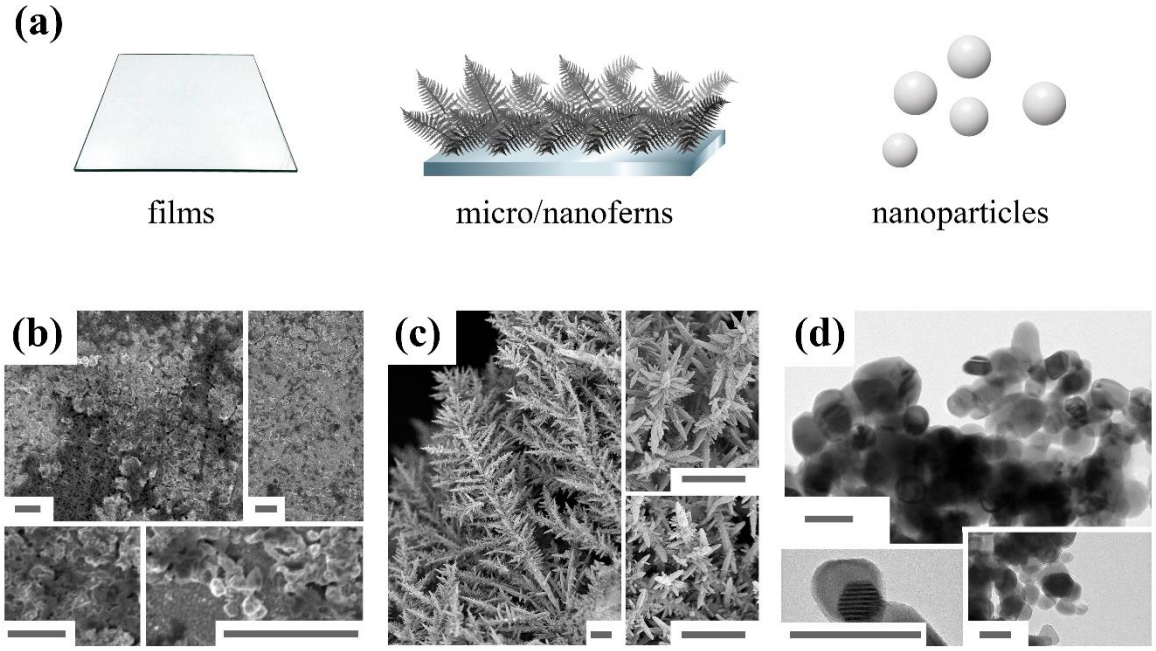

278

279 **Figure 1**: (a) Schematic representation of the different ZnO architectures. FE-SEM micrographs of (b)
280 the ZnO films (scale bar: 2 µm) and (c) the ZnO micro/nanoferns (scale bar: 5 µm). (d) HR-TEM mi-
281 crographs of the ZnO nanoparticles (scale bar: 100 nm).

282 As depicted in the FE-SEM micrographs, the chemically deposited ZnO films on glass formed a rough
283 layer with an average thickness of 40 ± 3 µm (**Figure 1b**). In contrast, the electrodeposited ZnO in
284 strong stirring conditions (high flux of oxygen and magnetic stirring) resulted in well-defined fractal
285 and dendritical ZnO micro/nanoferns (**Figure 1c**) with an average thickness of 53 ± 2 µm. On the other
286 hand, commercial ZnO nanoparticles were mainly spherical but showed a heterogeneous size distribu-
287 tion (diameters of 70 ± 26 nm) (**Figure 1d**).

288 The sulfidation process was easily observed macroscopically by the color change of the photocatalysts
289 from dark gray to golden (**Figure S1a**), which got darker for longer sulfidation times. Macroscopic color
290 changes were also observed in ZnO commercial nanoparticles when the ZnO@ZnS core@shell was
291 formed, changing from white to yellow (**Figure S1b**). At the microscopic level, important changes were
292 also seen in the architecture, morphology, and roughness of the photocatalyst. A substantial increase of
293 diameter in the central trunk and ramifications of micro/nanoferns – approximately 1.2 and 3.8 times

higher after 4 and 12 h of sulfidation, respectively – and a noticeable increase in the roughness (**Figure 2b-d, Figure S2**) was detected compared to the pristine ZnO micro/nanoferns, which can be explained by the Kirkendall effect (Serrà, et al., 2019; Ranjith, et al., 2018). The fractal and dendritical architecture was significantly reduced and damaged when the sulfidation was extended over 4 h (**Figure 2c, d**). In addition, the formation of ZnS shells with varying thicknesses depending on sulfidation time has also been confirmed by means of elemental mapping of the central trunk of ZnO@ZnS micro/nanoferns (**Figure S2c-e**), resulting in an increase in shell thickness when the sulfidation time increases. Note that, for a given sulfidation time, the ZnS shell thicknesses differ depending on the area of the micro/nanofern that is analyzed (i.e., central trunk, primary ramification, or secondary ramification) due to variations in surface reactivity and stability. Despite the increase in surface roughness, the overall micro/nanoferns architecture became more compact during the sulfidation process, which resulted in a significant reduction in the BET surface area values, falling from 68.2 m^2g^{-1} (ZnO micro/nanoferns) to 30.1 m^2g^{-1} (ZnO@ZnS(12h) micro/nanoferns) (**Table 1, Figure S3**). However, interestingly, the slight increase in roughness without affecting the architecture at short sulfidation times slightly increased the accessible surface area up to 70.4 m^2g^{-1} in the ZnO@ZnS(4h) micro/nanoferns, which may improve the photocatalytic activity by increasing the accessible reactive sites. In the case of the nanoparticles, a weak modification was observed in the particle size distribution –76 ± 21 nm for ZnO@ZnS nanoparticles– by the formation of a ZnS layer of approximately 8 nm in thickness (**Figure 2e**). In addition, **Table 1** shows that the ZnS to ZnO ratio increased considerably for longer sulfidation times, demonstrating that sulfidation is a volumetric process as a consequence of the thermally activated sulfur diffusion.

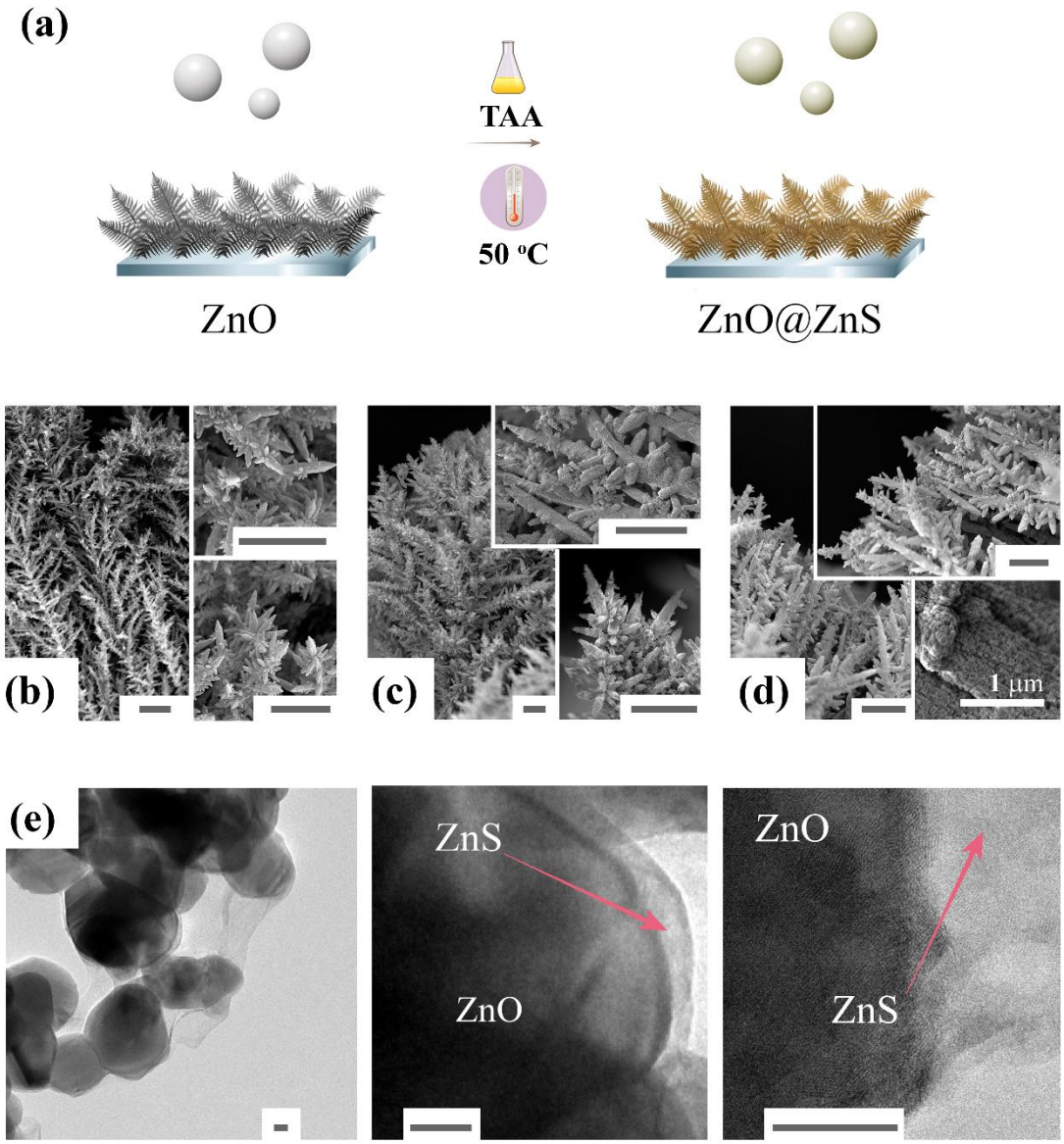

Figure 2: (a) Schematic representation of the sulfidation process. FE-SEM micrographs of (b) the ZnO@ZnS(4h), (c) ZnO@ZnS(8h), and (d) ZnO@ZnS(12h) micro/nanoferns. Scale bar: 5 μm. (e) HR-TEM micrographs of the ZnO@ZnS(4h) nanoparticles. Scale bar: 20 nm.

The X-ray diffraction pattern (XRD) of the ZnO architectures (**Figure S4**) matched perfectly with the standard hexagonal wurtzite ZnO structure (JCPDS card No. 36-1451). However, the XRD measurements showed that ZnO films had a (101) preferred orientation, while in the ZnO nanoparticles and micro/nanoferns had a (002) preferred orientation. After the sulfidation process, the formation of the ZnS layer was confirmed by the detection of two extra peaks, which perfectly corresponded to the cubic

ZnS blende structure (JCPDS card No. 65-1691), at $2\theta = 28.55^{o}$ (111) and 33.87^{o} (200). A significant reduction in the intensity of ZnO was also observed, with a higher reduction as the sulfidation time increased, due to the substitution of ZnO by ZnS. The obtained data confirmed the formation of a ZnS shell over the ZnO surface due to the volumetric substitution of ZnO by ZnS. Therefore, controlling the sulfidation time is crucial for synthesizing well-defined ZnO@ZnS core@shell architectures.

The UV-vis DRS spectra (**Figure S5**) of the ZnO photocatalysts (film, nanoparticles, and micro/nano-ferns) showed a strong absorption in the UV region and a significantly lower intensity in the visible region due to the wide band-gap of ZnO. After the sulfidation process, the absorption band of ZnO was extended to the visible domain due to the formation of a two-phase heterojunction. Interestingly, the 4h sulfidation process yielded the highest absorbance in the visible range. The large difference in the lattice parameters between ZnO and ZnS is responsible of generating a large mechanical stress at the interface. Such stress can induce drastic changes in the band structure with a substantial reduction of the bandgap, as it has been predicted by numerical calculations (Torabi, et al., 2015). The incorporation of the S atoms can also generate additional lattice imperfections giving rise to impurity levels within the band-gap. The optical band-gap of the ZnO-based photocatalysts (**Table 1**) was calculated using Tauc relation (**Figure S6**). Note that the obtained values agree well with the data reported in the literature (Serrà, et al., 2019; Ranjith, et al., 2018). It is worth noting that the largest bandgap reduction is observed for the ZnO@ZnS(4h) micro/nanoferns. The increase of the sulfidation time clearly favored the dominant optical behavior of the ZnS, thereby widening again the bandgap. The photoluminescence measurements (**Figure S7**) showed an important intensity increase in the visible and near-infrared regions for the ZnO@ZnS(4h) micro/nanoferns compared to the pristine structures. The luminescence intensity decays in the 8h sulfidated sample, probably due to the decrease of the lattice imperfections and the lower surface area of the micro/nano-ferns. In contrast, the deterioration of the fern-like structures for longer (12h) sulfidation time generated by the large mechanical stress in the structures causing cracks and fractures, resulted in an increase of the luminescence intensity compared to the 8h sulfidation time. On the other hand, the sulfidation of the nanoparticles induced a luminescence reduction after 4h sulfidation time. This is possibly due to the isotropic sulfidation dynamics in the dispersed nanoparticles under

agitation, which enables the formation of a ZnS shell with lower mechanical stress and the reduction in the number of defects.

352 **Table 1.** Ratios of ZnS to ZnO, BET surface area, band-gap energy, and natural sunlight photocatalytic efficiency of the ZnO-based photocatalysts (photocatalyst

353 dosage = 400 mg L^{-1}, Temperature = 30.0 ± 0.1 °C).

Photocatalyst	**ZnS to ZnO ratio / at. %**	**ZnS thickness / nm**	**BET surface area / m^2 g^{-1}**	**Band-gap energy / eV**	**Mineralization efficiency (fresh photocatalyst) / %**	**Mineralization efficiency (after 8th recycling cycles)**
ZnO film	-	-	8.1	3.24 ± 0.12	4.3 ± 0.5	2.2 ± 0.3
ZnO nanoparticles	-	-	51.2	3.28 ± 0.09	17.9 ± 0.1	11.2 ± 0.4
ZnO@ZnS(4h) nanoparticles	34.6 ± 1.2	8	54.7	2.93 ± 0.05	61.7 ± 0.9	49.8 ± 0.4
ZnO micro/nanoferns	-	-	68.2	3.30 ± 0.07	20.1 ± 0.4	12.9 ± 0.5
ZnO@ZnS(4h) micro/nanoferns	25.8 ± 1.2	50-90	70.4	2.77 ± 0.07	81.4 ± 0.3	79.9 ± 0.7
ZnO@ZnS(8h) micro/nanoferns	52.4 ± 1.2	90-170	54.2	2.96 ± 0.09	71.0 ± 0.6	68.2 ± 0.6
ZnO@ZnS(12h) micro/nanoferns	75.7 ± 1.2	350-400	30.1	3.17 ± 0.06	39.9 ± 0.9	37.2 ± 0.4

354

3.2. Photocatalytic efficiency of ZnO-based structures

The photocatalytic performance of each photocatalyst was evaluated by means of UV-filtered natural and simulated sunlight irradiation (see supporting information). As expected, the ZnO@ZnS core@shell photocatalysts with well-defined biomimetic micro/nanoferns exhibited excellent photocatalytic efficiency (**Tables 1 and S1**) in mineralizing a multi-pollutant solution. Moreover, the ZnO@ZnS core@shell(4h) micro/nanoferns showed excellent reusability and recyclability properties (**Table 1**), as the mineralization efficiency was virtually constant after their reuse for eight consecutive times. Note that the ZnO@ZnS core@shell(4h) nanoparticles exhibited worse recycling properties, possibly due to nanoparticle loss during the recycling process.

3.3. Reactive oxygen species identification

It is well known that ROS generated during the photocatalyst irradiation are not only efficient to mineralize organic compounds, but also to damage microorganisms. However, microorganisms must have direct contact/interaction with photocatalysts to suffer effective photo-damage due to the very short lifetime of the ROS. Although, hydroxyl radicals are the main actors in the photo-mineralization of organic pollutants and the photo-damage of microorganisms, oxygen superoxide ions and singlet oxygen can also be relevant in for both processes (Anastasescu, et al., 2018). To assess the role of the different ROS, we first investigated the kinetics and concentration of hydroxyl radicals using fluorescein salt as selective radical quencher (**Figure 3a**, **3b,** and **S8**). **Figure 3a** shows the time-dependent evolution of fluorescein concentration under simulated sunlight by following the photoluminescence peak at 515 nm (λ_{ex} = 303 nm). The kinetics of hydroxyl generation (**Figure 3b**) was evaluated by assuming zero order kinetics and equimolar reaction stoichiometry between hydroxyl radicals and fluorescein molecules. The kinetics of hydroxyl formation was also investigated in the absence of photocatalysts as the photolysis of water can also generate hydroxyl radicals. The hydroxyl formation by the ZnO@ZnS(4h) micro/nanoferns was approximately 45, 30, 1.8, 44, 1.8 and 2.6 times higher than that obtained for ZnO films, ZnO nanoparticles, ZnO@ZnS(4h) nanoparticles, ZnO, ZnO@ZnS(8h), and ZnO@ZnS(12h) micro/nanoferns, respectively. The photolytic formation of hydroxyl radicals from water was negligible,

as it was 380 times lower than that obtained for the ZnO@ZnS(4h) micro/nanoferns. Next, the formation of oxygen superoxide ions was determined by monitoring spectroscopically the reaction of XTT and oxygen superoxide ions (**Figure 3c**). As can be seen in **Figure 3c**, ZnO@ZnS core@shell photocatalysts presented a relatively low activity to generate oxygen superoxide ions compared to the ZnO photocatalysts. Note that superoxide ions have a low oxidation power, which provides a relatively low activity to mineralize the POPs or to damage the microorganism cell wall. In acidic media, the superoxide radical can react with protons to generate hydroxyl radicals. However, this process is negligible in alkaline solutions such as microalgae media. In addition, the formation of singlet oxygen molecules was monitored by determining the consumption of SOSG reagent (**Figure 3d**) and the formation of endoperoxide compound (**Figure 3e**). According to these experiments, ZnO@ZnS core@shell photocatalysts also presented a relatively low activity to produce singlet oxygen compared to ZnO. Consequently, the high mineralization efficiency of the ZnO@ZnS core@shell photocatalysts can be attributed to the high production of hydroxyl radicals, which can also damage microorganisms in direct contact to the photocatalysts.

3.4. Photostability and anti-photocorrosion of the different ZnO-based structures

A well-known problem of the ZnO-based photocatalysts is their high photocorrosion, which considerably affects their efficiency and potential use (Han, et al., 2014; Weng, et al., 2014). The photocorrosion triggers the release of Zn(II) ions (i.e., new pollutants) into water, which exert important negative effects on ecosystems, especially on biota. Therefore, for practical applications photocatalysts require high photocorrosion resistance, chemical stability, and high reusability.

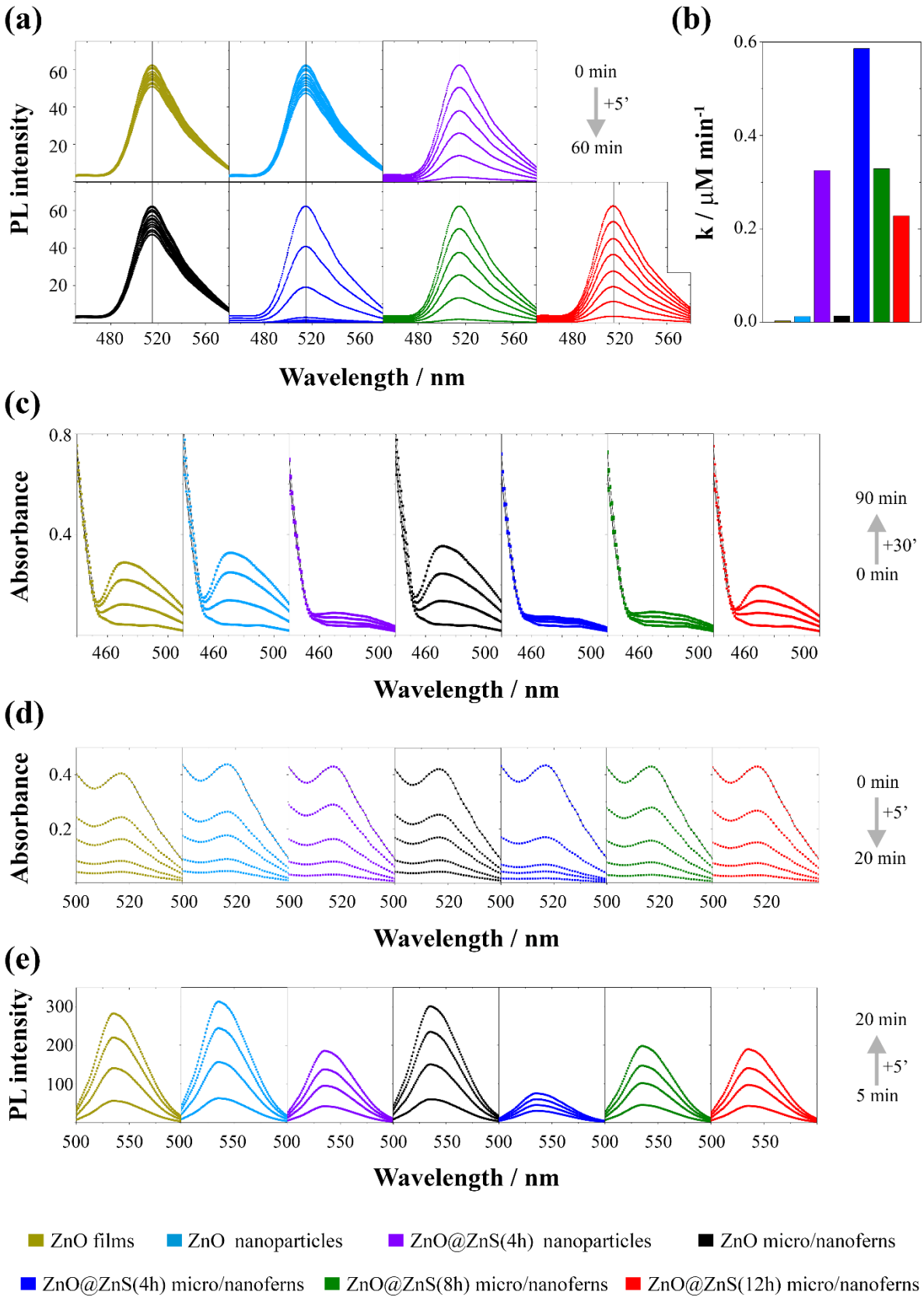

404

405 **Figure 3**: (a) Time-dependent photoluminescence spectra of 8 μM fluorescein (FL) and (b) kinetic con-

406 stant of hydroxyl radical formation using ZnO-based photocatalysts. Time-dependent UV-vis spectra of

(c) the formation of XTT-formazan, which indicates the formation of oxygen superoxide ions, and (d) SOSG consumption using ZnO-based photocatalysts. (e) Time-dependent photoluminescence spectra of endoperoxide formation, which indicate the formation of singlet oxygen, using ZnO-based photocatalysts. Photocatalyst dosage = 400 mg L^{-1}; temperature = 30.0 ± 0.1 ºC; irradiation: UV-filtered simulated sunlight (> 400 nm, light intensity of 678 ± 11 lx).

To evaluate the photostability of the ZnO-based photocatalysts, the time-dependent concentration of Zn(II) ions in the algal culture medium containing 400 mg L^{-1} of each photocatalyst was determined after an irradiation time of 96 h with UV-filtered simulated sunlight. As **Figure 4** shows, the photocorrosion mainly depends on the photocatalyst composition, being especially high in the case of unmodified ZnO films, nanoparticles and micro/nanoferns. Note that the Zn(II) concentration in aqueous media indicates the dissolution of 91%, 78%, and 76% of the ZnO film, the nanoparticles, and the micro/nanoferns, respectively. In addition, the photocatalyst shape and architecture also affects the photocorrosion effect, since nanoparticles and micro/nanoferns, which have larger surface area and a greater ability to trap light, present a lower photocorrosion than ZnO films. These results confirm that the photocorrosion activity is strongly related to crystal morphology (i.e., different facets) and the physical properties of the ZnO surface, having more photo-stability ZnO micro/nanomaterials with a (002) preferred orientation (Debroye, et al., 2017; Ishioka, et al., 2017). In contrast, ZnO@ZnS(4h) core@shell architectures exhibited excellent anti-photocorrosive properties, with a ZnO dissolution of less than 5%, due to the effective transfer of photogenerated holes from the ZnO core to the ZnS shell, both protecting the surface oxygen of ZnO from the solution and preventing the attack of the surface oxygen atom by the holes transported to the catalyst/solution interface (Torabi, et al., 2015, Yu, et al., 2015). However, after longer sulfidation times, the ZnS behavior predominates and, therefore, the photocorrosion activity is significantly increased, as expected from the well-known photo-instability of pure ZnS. Therefore, the photocorrosion resistance strongly depends on the shell thickness that serves as a protective coating. This behavior has also been observed in the case of the ZnS@ZnO core@shell photocatalysts (Serrà, et al., 2019; Ranjith, et al., 2018). The photocatalyst dissolution is clearly confirmed by observing the changes in the surface morphology of each photocatalyst after 96 h of continuous irradiation in a fresh algal culture medium.

As can be seen in **Figure S10,** the surface morphology of the ZnO micro/nanoferns exhibited a deterioration of the catalyst surface accompanied by the detachment of photocatalyst fragments after 96 h of continuous irradiation. On the other hand, only roughness increase was observed in the core@shell heterostructures, which was more relevant for the structures with longer sulfidation times. Therefore, the formation of a thin ZnS layer considerably increased the photocorrosion resistance, although the Zn(II) concentration in the solution raised when the sulfidation time was increased.

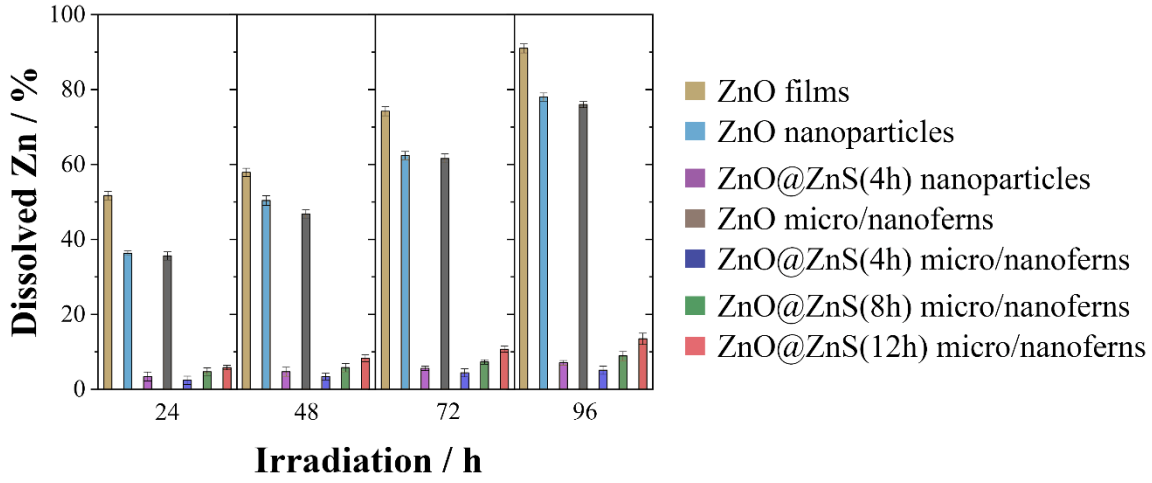

Figure 4: Percentage of dissolved Zn (relative to the initial amount of Zn in each ZnO-based photocatalyst) after the continuous irradiation of 400 mg L^{-1} of the ZnO-based photocatalysts in a fresh algae culture medium under UV-filtered simulated sunlight (temperature = 30.0 ± 0.1 ºC). Error bars indicate standard deviations of the four replicated experiments.

3.5. Ecotoxicological effects of the different ZnO-based photocatalysts on microalgae

Although the interaction of micro- and nano-structures with algae can favor microalgae growth, in general, photocatalysts can present negative effects on microalgae viability. Several studies have analyzed the effect of ZnO-based nanomaterials on plants, algae, and other living organisms, attributing ZnO toxicity mainly to the release of Zn(II) ions as a consequence of the poor photostability (Bondarenko, et al., 2013; Hou, et al., 2018; Aruoja, et al., 2009; Ma, et al., 2013; Miao, et al., 2010; Wong, et al., 2010). It is generally accepted that the ZnO toxicity is mainly produced by the solubilization of Zn(II) ions,

which form metal bindings to SH-groups of proteins, especially in the plasma membranes, and inhibit the cell or microorganisms growth. However, most studies ignore other important effects such as the aggregation or sedimentation of the nanostructures, or the organism-nanostructure interaction, thus attributing that ZnO-based nanomaterials have greater toxicity than bulk materials solely due to the solubilized Zn(II) ions (Bondarenko, et al., 2013; Hou, et al., 2018; Aruoja, et al., 2009; Ma, et al., 2013; Miao, et al., 2010; Wong, et al., 2010). However, we demonstrate here that the toxicity of ZnO-based photocatalysts is motivated by at least three different factors: (i) the release of inorganic toxic substances (e.g., Zn(II)) as a consequence of their poor chemical and photochemical stability, (ii) the mechanical effects as a consequence of the microalgae-photocatalyst interaction, in which the shape and catalyst fixation have an important role, and (iii) the photogeneration of ROS (Serrà, et al., 2019; Ranjith, et al., 2018).

The reduction in microalgae viability, biomass, and photosynthetic pigments of *Spirulina platensis* (**Figure 5**) demonstrated that the photocatalyst architecture and shape have a determining effect on microalgae viability. The percentage of maximum microalgae death at 96 h was 48.3±4.6 %, 72.5±3.9 %, 84.8±3.7 %, 88.8±1.2 %, and 91.7±1.7 %, at 25, 50, 100, 200, and 400 mg L^{-1} of ZnO nanoparticles, respectively. These values were approximately 1.7 and 2.6 times higher than those obtained with the same amount of ZnO micro/nanoferns and films, respectively. In addition, the reduction in biomass exhibited exactly the same trend as the microalgae viability. The different amounts of released Zn(II) due to the different surface areas and surface stability, significantly influenced the photocatalyst's toxicity on microalgae. The toxicity of unmodified ZnO photocatalysts was clearly indicated by the red and brown microalgae clumps after 96 h of incubation (**Figure S11**). However, toxicity did not depend exclusively on the release of Zn(II) ions; because the release rate of Zn(II) for films was approximately 1.2 times greater than that for nanoparticles and micro/nanoferns. The microalgae-photocatalyst interaction and the production of ROS also determined its toxicity. Microalgae-photocatalyst interaction can be achieved by the internalization of photocatalysts within the microalgae, which depends upon the type of microalgae and the size of photocatalyst, or by the simple physical contact between the entities. In the study reported here, no internalization of nanoparticles or micro/nanoferns fragments occurred after

96 h of incubation, since the electronic microscopy analysis of the residues resulting from the dissolution of dried microalgae did not present any photocatalyst fragments. Therefore, the greater toxicity of nanoparticles and micro/nanoferns can be explained by the sum of the release of Zn(II) ions, the greater interaction of the micro/nanoferns, especially the nanoparticles with the microalgae, and the photogeneration of ROS. Note that the effect of ROS also requires the direct physical interaction of microalgae and photocatalysts.

The significant effect of the Zn(II) release was clearly demonstrated when ZnO@ZnS core@shell micro/nanoferns were used since the loss in viability (400 mg L^{-1} of photocatalyst at 96 h of exposure) was approximately 5-6 times lower for ZnO@ZnS(4h), ZnO@ZnS(8h), and ZnO@ZnS(12h) micro/nanoferns, when compared with unmodified ZnO micro/nanoferns (**Figure 6**). The same behavior was also observed when ZnO@ZnS(4h) nanoparticles were used (**Figure S12**).

Regarding the architecture/shape effect, the comparison of ZnO@ZnS(4h) nanoparticles and micro/nanoferns show that the negative effects on microalgae were slightly higher for nanoparticles, despite having a virtually identical release of Zn(II) ions. Thus, the greater contact and interaction between the microalgae and the photocatalysts in the case of nanoparticles have greater negative effects on microalgae cultivation due to the photo-damage produced by the photogenerated ROS.

Concerning the fixation state, non-fixed ZnO@ZnS(4h) micro/nanoferns (i.e., detached from the fluorine-doped tin oxide film on a glass substrate) exhibited at least 3 times higher negative effect on all of the analyzed microalgae viability parameters compared to the fixed-micro/nanoferns, as can be seen in **Figure 6**. The interaction between the photocatalyst and the microalgae, and surely the mechanical effects (i.e., mechanical destruction) during the air bubbling of the cultivation process, also affected the development of *Spirulina* microalgae. Finally, it is worth comparing the results of the ZnO@ZnS micro/nanoferns for different sulfidation times. Although the release of Zn(II) was substantially more pronounced for long sulfidation times, these structures showed a slightly lower viability reduction compared to the ZnO@ZnS(4h) micro/nanoferns. The slight increase of the ecotoxicity in the later structure can then be attributed to its enhanced photocatalytic efficacy to produce hydroxyl radicals, which are the

main mediators of the efficient pollutant (photo)mineralization (Serrà, et al., 2019). When the ZnO@ZnS(4h) micro/nanoferns were fixed, the effect was weak due to the very short lifetime of the hydroxyl radicals. However, the detrimental effect could be more pronounced when the micro/nanoferns were not fixed, thereby enabling a closer interaction with the algae.

The quantification of the photosynthetic pigments can also provide important information to determine the effects that inhibit microalgae growth. To show effect of the different ZnO and ZnO@ZnS structures, the variation in the content of photosynthetic chlorophyll-a, carotenoids, and phycocyanin pigments was also evaluated, as Zn(II) can replace Mg(II) in chlorophyll molecules, thereby inhibiting the photosynthesis process. However, it should be taken into account that the effects of Zn(II) concentration might be complex. Low Zn(II) concentrations can stimulate the production of photosynthetic molecules, but the production inhibition is significant when a certain amount is exceeded, thus decreasing the concentration of chlorophyll-a and carotenoids. In addition, the Zn(II) concentration can present also significant effects on the photosynthesis of phycocyanin, possibly as a consequence of the Zn(II) ions blocking the enzyme activity in the photosynthetic synthesis route (Bondarenko, et al., 2013; Hou, et al., 2018; Aruoja, et al., 2009; Ma, et al., 2013; Miao, et al., 2010; Wong, et al., 2010). In the case of the ZnO and ZnO@ZnS structures, the reduction of the photosynthetic pigments (**Figure 5c-e, S13**, and **S14**) followed the same trend as microalgae viability and the reduction of biomass: the longer the exposure time and the concentration, the greater the effect due to the higher amount of released Zn(II). Therefore, all the analyzed parameters to determine the ecotoxicological effects of ZnO-based photocatalysts followed the same trend. The results show that Zn(II) release is the main toxicity effect, but shape, architecture, fixation, and ROS photogeneration must be considered as well, as discussed above.

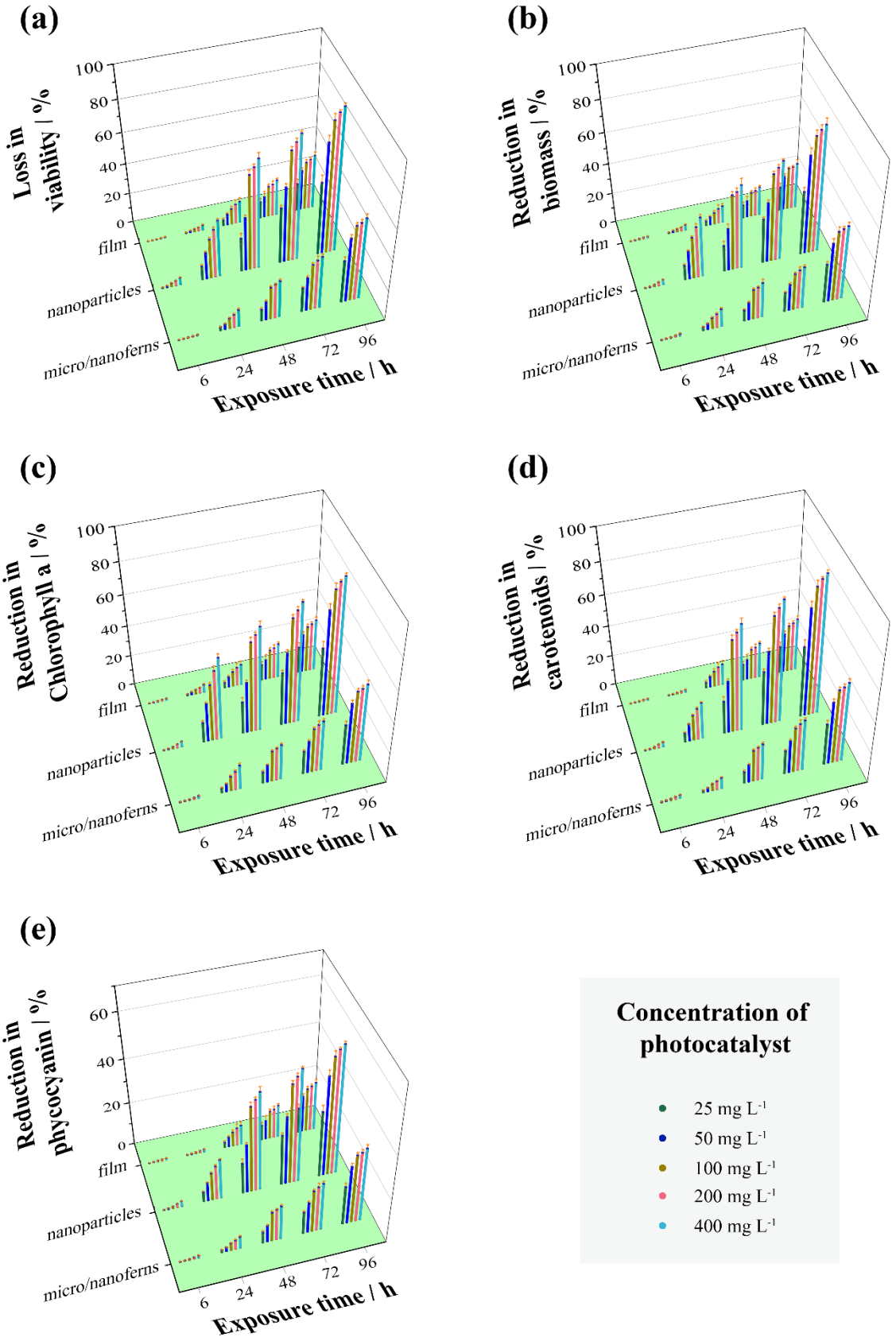
(a)
Loss in viability | %
(b)
Reduction in biomass | %
(c)
Reduction in Chlorophyll a | %
(d)
Reduction in carotenoids | %
(e)
Reduction in phycocyanin | %
film
nanoparticles
micro/nanoferns
Exposure time | h
6
24
48
72
96
Concentration of photocatalyst
25 mg L-1
50 mg L-1
100 mg L-1
200 mg L-1
400 mg L-1

528

Figure 5: Percentage of loss in (a) the microalgae viability, (b) the microalgae biomass, (c) the chlorophyll-a of the microalgae, (d) the carotenoids of the microalgae, and (e) the phycocyanin pigment of the microalgae for the treatment with 25, 50, 100, 200, and 400 mg L^{-1} of ZnO films, nanoparticles, and bioinspired micro/nanoferns after an exposure time of 6, 24, 48, 72, and 96 h. The microalgae cultures were irradiated 8 h per day with continuous simulated sunlight (light intensity of 740 ± 15 lx), starting the first irradiation cycle when photocatalysts were introduced in microalgae culture. Percentages are relative to the control (microalgae culture without catalyst) cultivated in the same experimental conditions. Error bars indicate standard deviations of the four replicated experiments.

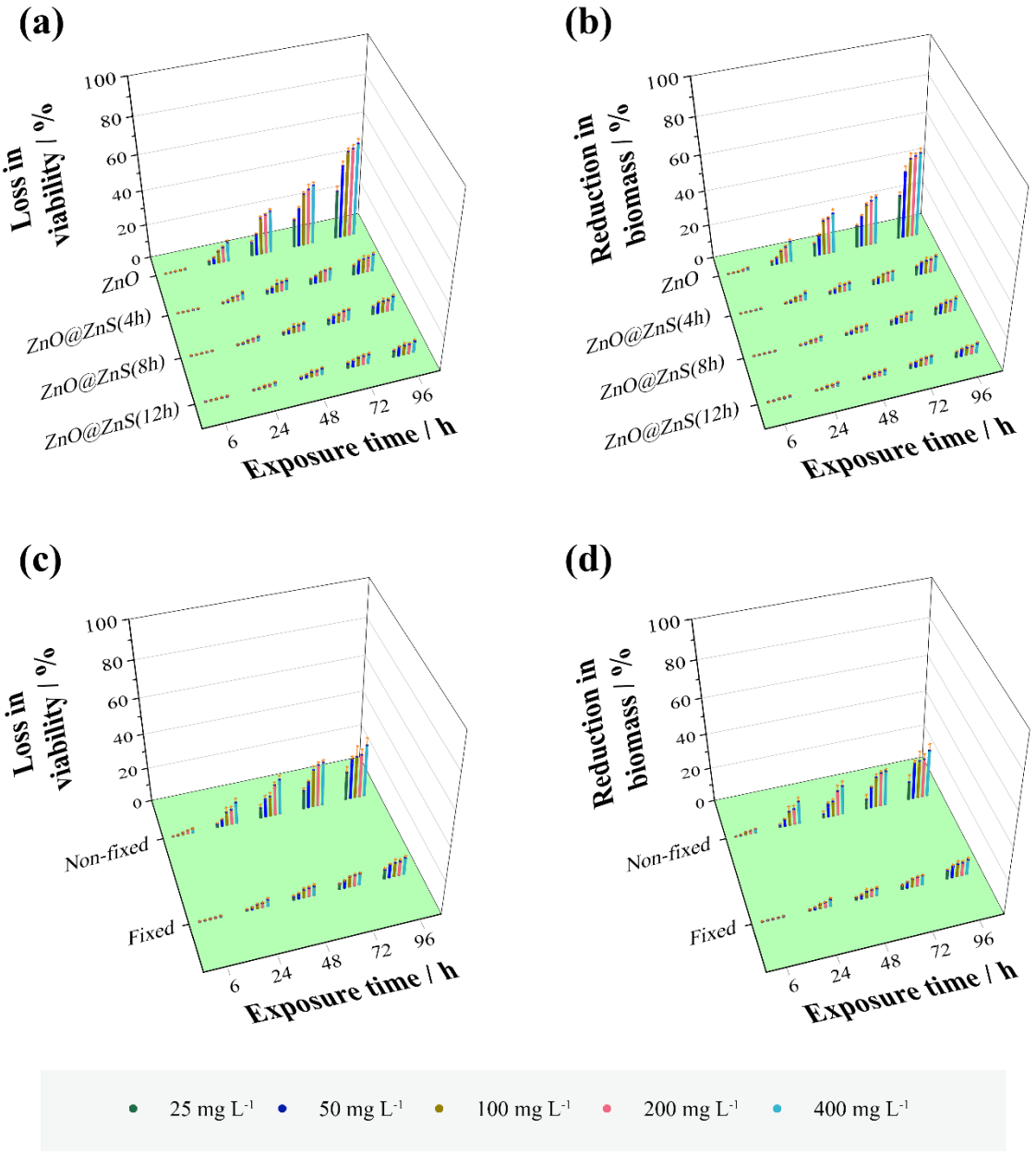

537

538 **Figure 6:** Percentage of loss in (a, c) the microalgae viability and (b, d) the microalgae biomass reduc-
539 tion of microalgae for the treatment with 25, 50, 100, 200, and 400 mg L^{-1} of ZnO-based bioinspired
540 micro/nanoferns after exposure times of 6, 24, 48, 72, and 96 h. The microalgae cultures were irradiated
541 8 h per day with continuous simulated sunlight (light intensity of 740 ± 15 lx), starting the first irradia-
542 tion cycle when photocatalysts were introduced in microalgae culture. Percentages are relative to the
543 control (microalgae culture without catalyst) cultivated in the same experimental conditions. Error bars
544 indicate standard deviations of the four replicated experiments.

4. Conclusion

Realizing efficient and totally clean photocatalysts for water decontamination requires the development of new materials with minimal impact on ecosystems, which involves integrating improved photocatalytic performance with reduced ecotoxicological effects throughout the catalyst life cycle. With this in mind, the effects of architecture, chemical composition, and fixation on the ecotoxicity of different ZnO-based sunlight photocatalysis on microalgae were analyzed and discussed, and the following conclusions can be highlighted:

(i) Effects of architecture. ZnO micro/nanofern architectures had ecotoxicological effects on microalgae comparable to those of film architectures but significantly lower than nanoparticles. Photocatalyst architecture is also relevant to avoid or promote (depending on the application) the interaction between the microorganisms and the photocatalysts. Such interactions determine the photo-inactivation and photo-damage produced by the generated ROS under sunlight irradiation.

(ii) Effects of composition. We show that controlling the ZnS shell thickness is critical, since long sulfidation times affect the surface morphology, photocorrosion resistance, and photocatalytic performance of the micro/nanofern architecture. Most importantly, the reduced photocorrosion enabled a large decrease in the release of Zn(II) ions into the environment, thus improving the reusability and recyclability of the core@shell photocatalysts for water remediation and causing a remarkably lower ecotoxicity on microalgae – at least five times lower – relative to non-modified ZnO. However, ZnO@ZnS core@shell photocatalysts produced a significantly greater number of hydroxyl radicals, which can play important roles in the photo-inactivation and photo-damage of microorganisms when photocatalysts and microorganisms are in direct contact.

(iii) Effects of fixation. Fixation of the photocatalysts also facilitated their recyclability and reduced the interaction with microalgae. Most importantly, the reduced photochemical and mechanical interactions in micro/nanofern architectures improved the viability reduction at least three-fold.

In conclusion, the optimized ZnO@ZnS(4h) fern architectures are excellent ecofriendly candidates for photocatalytic water remediation in complex saline and biological media given their excellent

mineralization efficiency, outstanding photostability, photocorrosion resistance, and minimal ecotoxicological effects on aquatic biota.

Acknowledgments

This work was partially supported by the Metrohm foundation. Partial funding from the 2017-SGR-292 project from the *Generalitat de Catalunya*, and the PCIN2016-093 and TEC2017-85059-C3-2-R projects (co-financed by the *Fondo Europeo de Desarrollo Regional*, FEDER) from the Spanish *Ministerio de Economía y Competitividad* (MINECO) is also acknowledged. ICN2 is funded by the CERCA Programme/*Generalitat de Catalunya*. ICN2 also acknowledges the support from the *Severo Ochoa* Program (MINECO, Grant No. SEV-2017-0706). Albert Serrà would like to acknowledge funding from the EMPAPOSTDOCS-II program. The EMPAPOSTDOCS-II programme has received funding from the European Union's Horizon 2020 research and innovation programme under the Marie Skłodowska-Curie grant agreement number 754364. Yue Zhang acknowledges the China Scholarship Council (CSC) for financial support (201608310112).

Appendix A. Supplementary data

Supplementary material related to this article can be found, in the online version, a

References

Anastasescu, C., Negrila, C., Angelescu, D.G., Atkinson, I., Anastasescu, M., Spataru, N., Zaharescu, M., Balint, I., 2018. Particularities of photocatalysis and formation of reactive oxygen species on insulators and semiconductors: Cases of SiO_2, TiO_2 and their composite SiO_2-TiO_2. Catal. Sci. Technol. 8, 5657–5668. https://doi.org/10.1039/c8cy00991k

Arshad, A., Iqbal, J., Siddiq, M., Mansoor, Q., Ismail, M., Mehmood, F., Ajmal, M., Abid, Z., 2017. Graphene nanoplatelets induced tailoring in photocatalytic activity and antibacterial characteristics of MgO/graphene nanoplatelets nanocomposites. J. Appl. Phys. 121. https://doi.org/10.1063/1.4972970

Aruoja, V., Dubourguier, H.C., Kasemets, K., Kahru, A., 2009. Toxicity of nanoparticles of CuO, ZnO and TiO2to microalgae Pseudokirchneriella subcapitata. Sci. Total Environ. 407, 1461–1468. https://doi.org/10.1016/j.scitotenv.2008.10.053

598 Batista, L.M.B., dos Santos, A.J., da Silva, D.R., Alves, A.P. de M., Garcia-Segura, S., Martínez-
599 Huitle, C.A., 2017. Solar photocatalytic application of NbO2OH as alternative photocatalyst for
600 water treatment. Sci. Total Environ. 596–597, 79–86. https://doi.org/10.1016/j.sci-
601 totenv.2017.04.019

602 Bennett, A., Bogorad, L., 1973. Complementary Chromatic Adaptation in a Filamentous Blue-Green
603 Alga. J. Cell Biol. 58, 419 LP-435. https://doi.org/10.1083/jcb.58.2.419

604 Bettinetti, R., Quadroni, S., Manca, M., Piscia, R., Volta, P., Guzzella, L., Roscioli, C., Galassi, S.,
605 2012. Seasonal fluctuations of DDTs and PCBs in zooplankton and fish of Lake Maggiore
606 (Northern Italy). Chemosphere 88, 344–351. https://doi.org/10.1016/j.chemosphere.2012.03.009

607 Bondarenko, O., Juganson, K., Ivask, A., Kasemets, K., Mortimer, M., Kahru, A., 2013. Toxicity of
608 Ag, CuO and ZnO nanoparticles to selected environmentally relevant test organisms and mam-
609 malian cells in vitro: A critical review. Arch. Toxicol. 87, 1181–1200.
610 https://doi.org/10.1007/s00204-013-1079-4

611 Chong, M.N., Jin, B., Chow, C.W.K., Saint, C., 2010. Recent developments in photocatalytic water
612 treatment technology: A review. Water Res. 44, 2997–3027. https://doi.org/10.1016/j.wa-
613 tres.2010.02.039

614 Debroye, E., Van Loon, J., Yuan, H., Janssen, K.P.F., Lou, Z., Kim, S., Majima, T., Roeffaers, M.B.J.,
615 2017. Facet-Dependent Photoreduction on Single ZnO Crystals. J. Phys. Chem. Lett. 8, 340–346.
616 https://doi.org/10.1021/acs.jpclett.6b02577

617 Deniz, F., Saygideger, S.D., Karaman, S., 2011. Response to copper and sodium chloride excess in
618 Spirulina sp. (Cyanobacteria). Bull. Environ. Contam. Toxicol. 87, 11–15.
619 https://doi.org/10.1007/s00128-011-0300-5

620 Dere, S., Gunes, T., Sivaci, R., 1998. Spectrophotometric Determination of Chlorophyll - A, B and
621 Total Carotenoid Contents of Some Algae Species Using Different Solvents. Turkey J. Bot. 22,
622 13–17. https://doi.org/10.1080/19393550802541200

623 Djearamane, S., Lim, Y.M., Wong, L.S., Lee, P.F., 2018. Cytotoxic effects of zinc oxide nanoparticles
624 on cyanobacterium *Spirulina (Arthrospira) platensis*. PeerJ 6, e4682.
625 https://doi.org/10.7717/peerj.4682

626 Everaert, G., De Laender, F., Goethals, P.L.M., Janssen, C.R., 2015. Relative contribution of persis-
627 tent organic pollutants to marine phytoplankton biomass dynamics in the North Sea and the Kat-
628 tegat. Chemosphere 134, 76–83. https://doi.org/10.1016/j.chemosphere.2015.03.084

629 Fu, F., Wang, Q., 2011. Removal of heavy metal ions from wastewaters: A review. J. Environ. Ma-
630 nage. 92, 407–418. https://doi.org/10.1016/j.jenvman.2010.11.011

631 Han, C., Yang, M.Q., Weng, B., Xu, Y.J., 2014. Improving the photocatalytic activity and anti-photo-
632 corrosion of semiconductor ZnO by coupling with versatile carbon. Phys. Chem. Chem. Phys.
633 16, 16891–16903. https://doi.org/10.1039/c4cp02189d

634 Harris, T.D., Smith, V.H., 2016. Do persistent organic pollutants stimulate cyanobacterial blooms? Inl.
635 Waters 6, 124–130. https://doi.org/10.5268/IW-6.2.887

636 Hatamie, A., Khan, A., Golabi, M., Turner, A.P.F., Beni, V., Mak, W.C., Sadollahkhani, A., Alnoor,
637 H., Zargar, B., Bano, S., Nur, O., Willander, M., 2015. Zinc Oxide Nanostructure-Modified

638 Textile and Its Application to Biosensing, Photocatalysis, and as Antibacterial Material.
639 Langmuir 31, 10913–10921. https://doi.org/10.1021/acs.langmuir.5b02341

640 Hou, J., Wu, Y., Li, X., Wei, B., Li, S., Wang, X., 2018. Toxic effects of different types of zinc oxide
641 nanoparticles on algae, plants, invertebrates, vertebrates and microorganisms. Chemosphere 193,
642 852–860. https://doi.org/10.1016/j.chemosphere.2017.11.077

643 Ishioka, J., Kogure, K., Ofuji, K., Kawaguchi, K., Jeem, M., Kato, T., Shibayama, T., Watanabe, S.,
644 2017. In situ direct observation of photocorrosion in ZnO crystals in ionic liquid using a laser-
645 equipped high-voltage electron microscope. AIP Adv. 7. https://doi.org/10.1063/1.4979726

646 Jury, W.A., Vaux, H.J., 2007. The Emerging Global Water Crisis: Managing Scarcity and Conflict Be-
647 tween Water Users. Adv. Agron. 95, 1–76. https://doi.org/10.1016/S0065-2113(07)95001-4

648 Jury, W.A., Vaux, H.J., 2007. The Emerging Global Water Crisis: Managing Scarcity and Conflict Be-
649 tween Water Users. Adv. Agron. 95, 1–76. https://doi.org/10.1016/S0065-2113(07)95001-4

650 Khan, M.S., Zaidi, R., Goel, R., Musarrat, J., 2011 Biomanagement of metal-contaminated soild,
651 Spinger. https://doi.org/10.1007/978-94-007-1914-9

652 Khan, M.U., Mitchell, K., 1987. Chlorophylls Carotenoids. Methods Enzymol. 148, 350–382.
653 https://doi.org/10.1016/0076-6879(87)48036-1

654 Lee, K.M., Lai, C.W., Ngai, K.S., Juan, J.C., 2016. Recent developments of zinc oxide based photo-
655 catalyst in water treatment technology: A review. Water Res. 88, 428–448.
656 https://doi.org/10.1016/j.watres.2015.09.045

657 Liu, J., Wang, Y., Ma, J., Peng, Y., Wang, A., 2018. A review on bidirectional analogies between the
658 photocatalysis and antibacterial properties of ZnO. J. Alloys Compd. 783, 898–918.
659 https://doi.org/10.1016/j.jallcom.2018.12.330

660 Lone, J.A., Kumar, A., Kundu, S., Lone, F.A., Suseela, M.R., 2013. Characterization of tolerance limit
661 in spirulina platensis in relation to nanoparticles. Water. Air. Soil Pollut. 224.
662 https://doi.org/10.1007/s11270-013-1670-6

663 Ma, H., Williams, P.L., Diamond, S.A., 2013. Ecotoxicity of manufactured ZnO nanoparticles - A re-
664 view. Environ. Pollut. 172, 76–85. https://doi.org/10.1016/j.envpol.2012.08.011

665 Malato, S., Fernández-Ibáñez, P., Maldonado, M.I., Blanco, J., Gernjak, W., 2009. Decontamination
666 and disinfection of water by solar photocatalysis: Recent overview and trends. Catal. Today 147,
667 1–59. https://doi.org/10.1016/j.cattod.2009.06.018

668 Mani, D., Kumar, C., 2014. Biotechnological advances in bioremediation of heavy metals contami-
669 nated ecosystems: An overview with special reference to phytoremediation. Int. J. Environ. Sci.
670 Technol. 11, 843–872. https://doi.org/10.1007/s13762-013-0299-8

671 Maule, A., Wright, S.J.L., 1984. Herbicide effects on the population growth of some green algae and
672 cyanobacteria. J. Appl. Bacteriol. 57, 369–379. https://doi.org/10.1111/j.1365-
673 2672.1984.tb01403.x

674 Miao, A.J., Zhang, X.Y., Luo, Z., Chen, C.S., Chin, W.C., Santschi, P.H., Quigg, A., 2010. Zinc ox-
675 ide-engineered nanoparticles: Dissolution and toxicity to marine phytoplankton. Environ. Toxi-
676 col. Chem. 29, 2814–2822. https://doi.org/10.1002/etc.340

677 Mizuta, T., Ishibashi, T., Minemoto, T., Takakura, H., Hamakawa, Y., 2006. Chemical deposition of
678 zinc oxide thin films on silicon substrate. Thin Solid Films 515, 2458–2463.
679 https://doi.org/10.1016/j.tsf.2006.06.035

680 Moraes, C.C., Sala, L., Cerveira, G.P., Kalil, S.J., 2011. C-Phycocyanin extraction from Spirulina
681 platensis Wet. Biomass. 28, 45–49. http://dx.doi.org/10.1590/S0104-66322011000100006

682 Moreira, F.C., Boaventura, R.A.R., Brillas, E., Vilar, V.J.P., 2017. Electrochemical advanced oxida-
683 tion processes: A review on their application to synthetic and real wastewaters. Appl. Catal. B
684 Environ. 202, 217–261. https://doi.org/10.1016/j.apcatb.2016.08.037

685 Mortimer, M., Kasemets, K., Kahru, A., 2010. Toxicity of ZnO and CuO nanoparticles to ciliated pro-
686 tozoa Tetrahymena thermophila. Toxicology 269, 182–189.
687 https://doi.org/10.1016/j.tox.2009.07.007

688 Ranjith, K.S., Castillo, R.B., Sillanpaa, M., Rajendra Kumar, R.T., 2018. Effective shell wall thickness
689 of vertically aligned ZnO-ZnS core-shell nanorod arrays on visible photocatalytic and photo
690 sensing properties. Appl. Catal. B Environ. 237, 128–139. https://doi.org/10.1016/j.ap-
691 catb.2018.03.099

692 Serrà, A., Zhang, Y., Sepúlveda, B., Gómez, E., Nogués, J., Michler, J., Philippe, L., 2019. Highly ac-
693 tive ZnO-based biomimetic fern-like microleaves for photocatalytic water decontamination using
694 sunlight. Appl. Catal. B Environ. 248, 129–146. https://doi.org/10.1016/j.apcatb.2019.02.017

695 Singh, J.S., Seneviratne, G., Health, M.C., 2017 Agro-Environmental Sustainability. Springer.
696 https://doi.org/10.1007/978-3-319-49727-3

697 Subashchandrabose, S.R., Ramakrishnan, B., Megharaj, M., Venkateswarlu, K., Naidu, R., 2013. Mix-
698 otrophic cyanobacteria and microalgae as distinctive biological agents for organic pollutant deg-
699 radation. Environ. Int. 51, 59–72. https://doi.org/10.1016/j.envint.2012.10.007

700 T, R., McMullan, R, M., P, N., 2011. Remediation of dyes in textile effluent: a critical review on cur-
701 rent treatment technologies with a proposed alternative. Bioresour Technol 77, 247–255.
702 https://doi.org/10.1016/S0960-8524(00)00080-8

703 Torabi, A., Staroverov, V.N., 2015. Band Gap Reduction in ZnO and ZnS by Creating Layered
704 ZnO/ZnS Heterostructures. J. Phys. Chem. Lett. 6, 2075–2080.
705 https://doi.org/10.1021/acs.jpclett.5b00687

706 Vessalli, B.A., Zito, C.A., Perfecto, T.M., Volanti, D.P., Mazon, T., 2017. ZnO nanorods/graphene ox-
707 ide sheets prepared by chemical bath deposition for volatile organic compounds detection. J. Al-
708 loys Compd. 696, 996–1003. https://doi.org/10.1016/j.jallcom.2016.12.075

709 Wang, C.Y., Fu, C.C., Liu, Y.C., 2007. Effects of using light-emitting diodes on the cultivation of
710 Spirulina platensis. Biochem. Eng. J. 37, 21–25. https://doi.org/10.1016/j.bej.2007.03.004

711 Weng, B., Yang, M.Q., Zhang, N., Xu, Y.J., 2014. Toward the enhanced photoactivity and photosta-
712 bility of ZnO nanospheres via intimate surface coating with reduced graphene oxide. J. Mater.
713 Chem. A 2, 9380–9389. https://doi.org/10.1039/c4ta01077a

714 Wong, S.W.Y., Leung, P.T.Y., Djurišić, A.B., Leung, K.M.Y., 2010. Toxicities of nano zinc oxide to
715 five marine organisms: Influences of aggregate size and ion solubility. Anal. Bioanal. Chem.
716 396, 609–618. https://doi.org/10.1007/s00216-009-3249-z

Yadav, H.M., Kim, J.S., Pawar, S.H., 2016. Developments in photocatalytic antibacterial activity of nano TiO2: A review. Korean J. Chem. Eng. 33, 1989–1998. https://doi.org/10.1007/s11814-016-0118-2

Yu, L., Chen, W., Li, D., Wang, J., Shao, Y., He, M., Wang, P., Zheng, X., 2015. Applied Catalysis B : Environmental Inhibition of photocorrosion and photoactivity enhancement for ZnO via specific hollow ZnO core / ZnS shell structure. Applied Catal. B, Environ. 164, 453–461. https://doi.org/10.1016/j.apcatb.2014.09.055

Highly reduced ecotoxicity of ZnO-based micro/nanostructures on aquatic biota: Influence of architecture, chemical composition, fixation, and photocatalytic efficiency

Albert Serrà [‖,*], Yue Zhang [&], Borja Sepúlveda [&], Elvira Gómez [$, @], Josep Nogués [&, #], Johann Michler [‖], Laetitia Philippe [‖]

[‖] Empa, Swiss Federal Laboratories for Materials Science and Technology, Laboratory for Mechanics of Materials and Nanostructures, Feuerwerkerstrasse 39, CH-3602 Thun, Switzerland.

[&] Catalan Institute of Nanoscience and Nanotechnology (ICN2), CSIC and BIST, Campus UAB, Bellaterra, E-08193 Barcelona, Spain.

[$] Grup d'Electrodeposició de Capes Primes i Nanoestructures (GE-CPN), Departament de Ciència de Materials i Química Física, Universitat de Barcelona, Martí i Franquès, 1, E-08028, Barcelona, Catalonia, Spain.

[@] Institute of Nanoscience and Nanotechnology (IN^{2}UB), Universitat de Barcelona, Barcelona, Catalonia, Spain.

[#] ICREA, Pg. Lluís Companys 23, E-08010, Barcelona, Spain.

Corresponding author: albert.serraramos@empa.ch (A.S.)

Photograph of ZnO-based photocatalysts

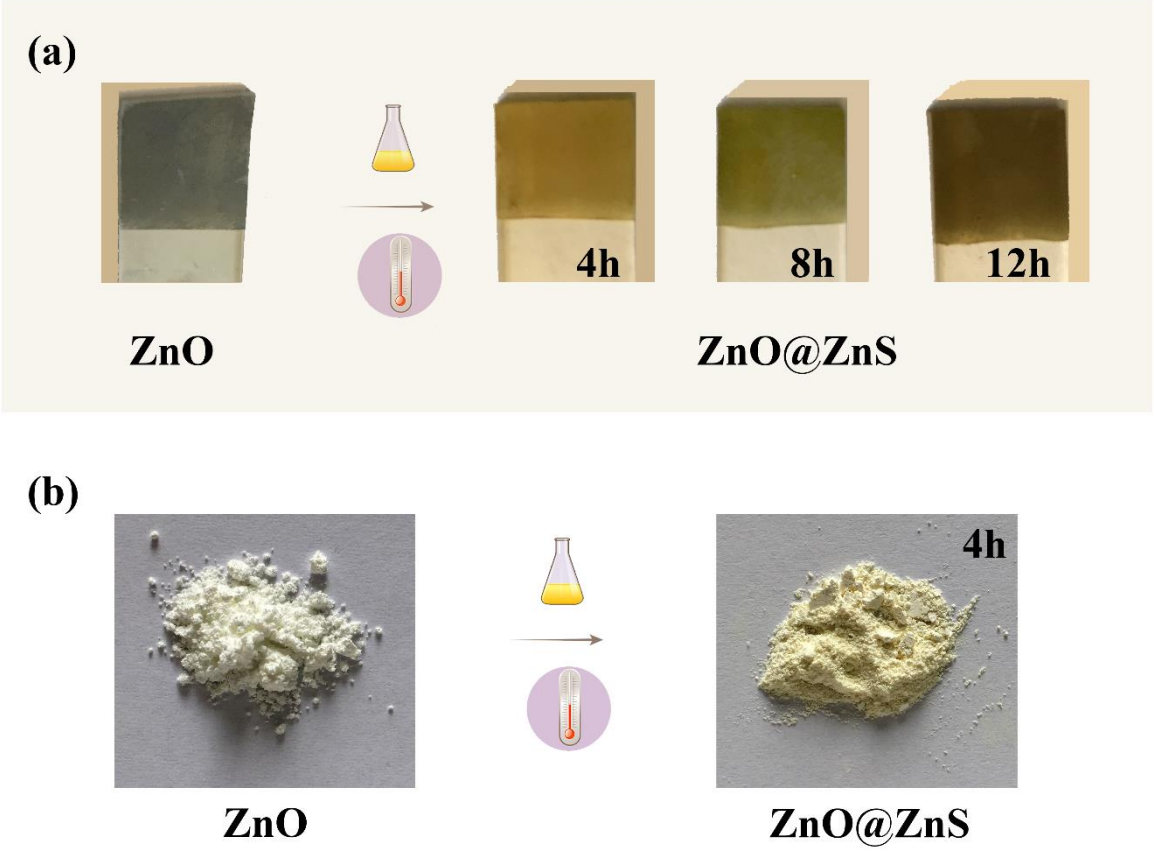

Figure S1: Photograph of (a) the as-prepared ZnO-based ferns and (b) the ZnO-based nanoparticles.

Scanning electron microscopy images of ZnO and ZnO@ZnS(12h) nano/microferns

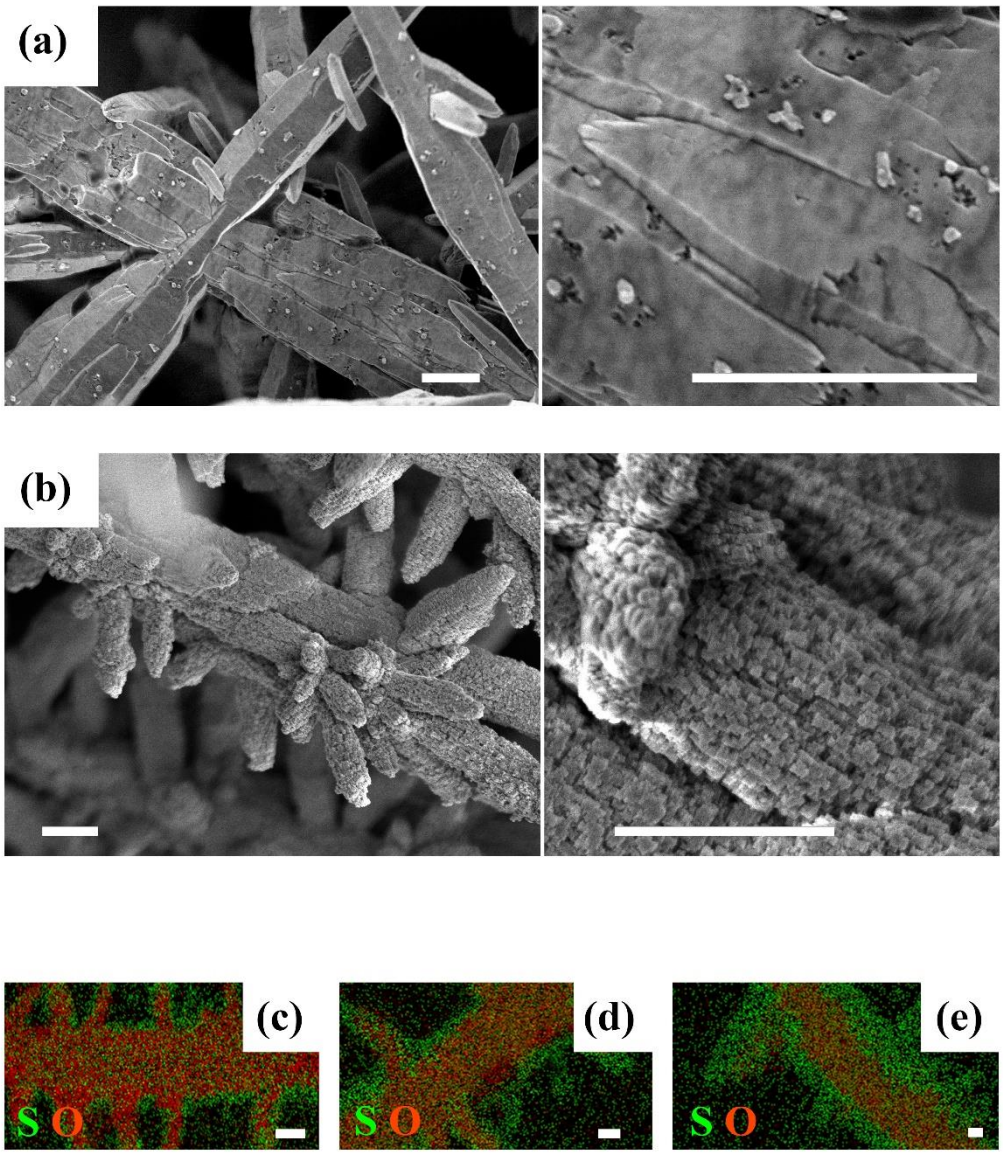

Figure S2: Representative FE-SEM micrographs of (a) the ZnO and (b) the ZnO@ZnS(12h) surfaces of the micro/nanoferns. Scale bar: 1 μm. EDS mapping of (c) the ZnO@ZnS(4h), (d)the ZnO@ZnS(8h), and (e) the ZnO@ZnS(12h) micro/nanoferns. Scale bar: 400 nm.

Brunauer-Emmett-Teller surface areas

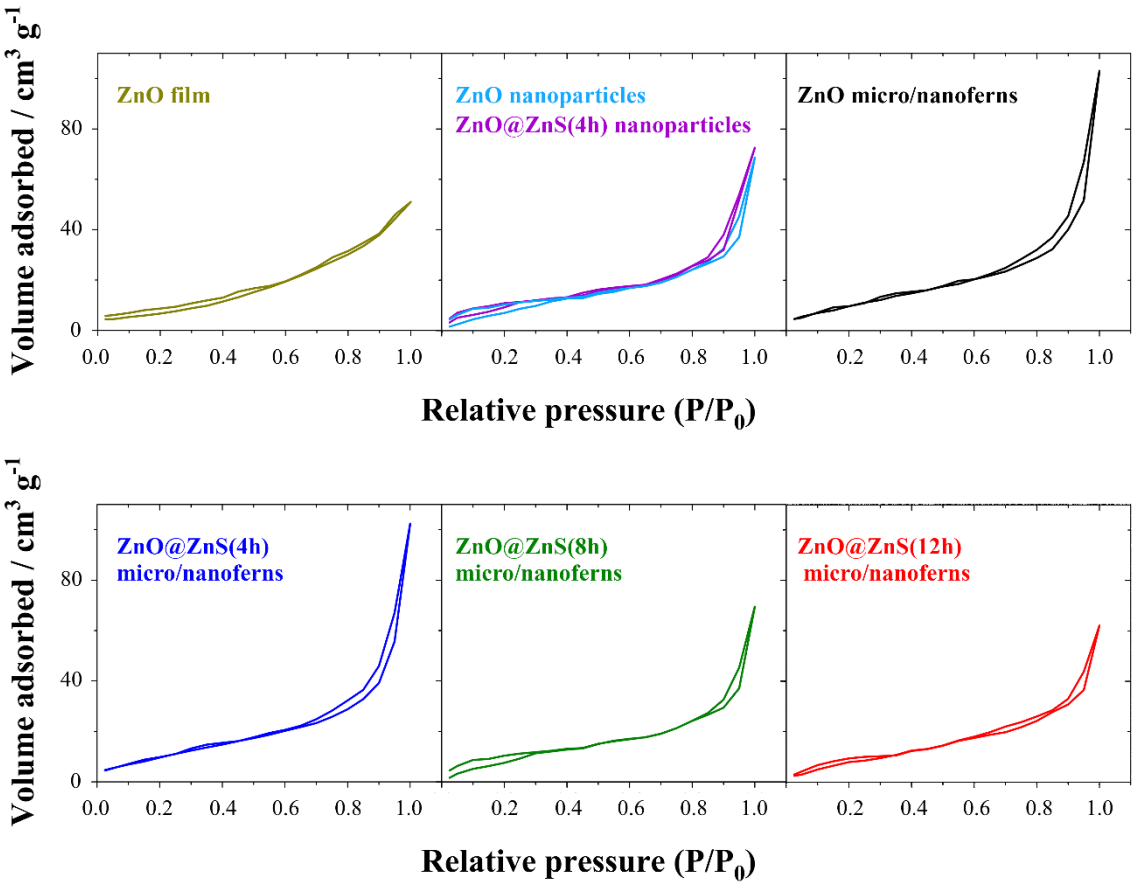

Figure S3: N_2 adsorption-desorption isotherms of the different ZnO-based photocatalysts.

XRD of ZnO-based photocatalysts

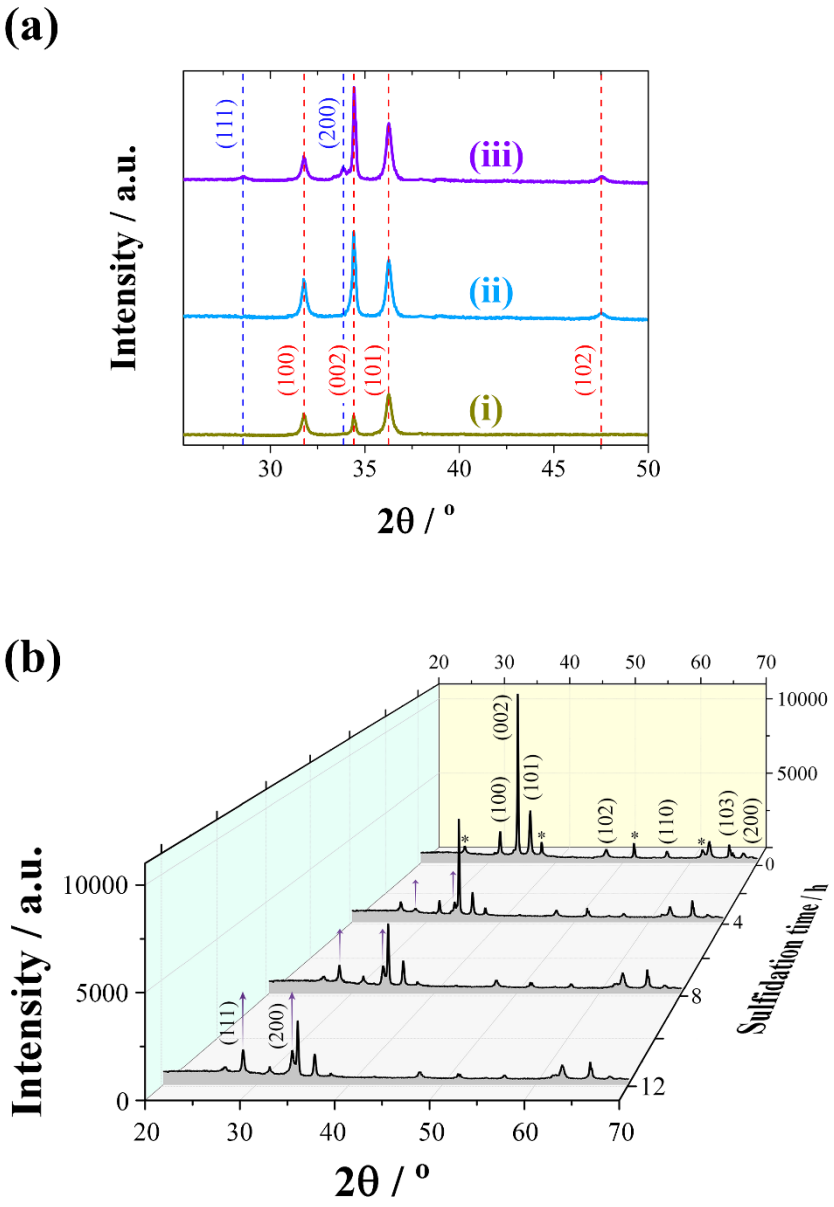

Figure S4: (a) XRD patterns of (i) the ZnO films and (ii) the ZnO nanoparticles and (iii) the ZnO@ZnS(4h) nanoparticles. (b) XRD patterns of ZnO-based bioinspired fern-shape microleaves. The diffraction peaks that correspond to the fluorine-doped tin oxide substrate structures are indicated with an *. The main peaks corresponding to ZnO and ZnS are highlighted by ↑.

UV-vis DRS absorption of ZnO-based photocatalysts

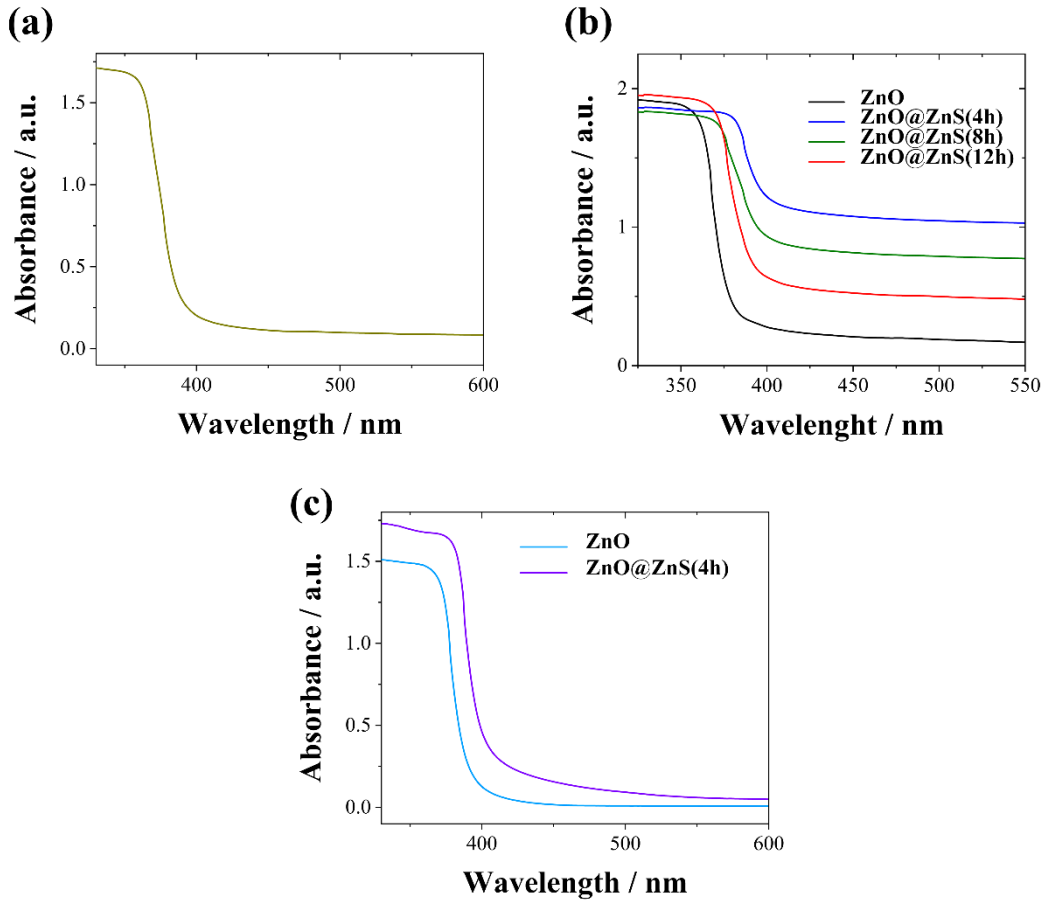

Figure S5: UV-vis DRS absorption spectra of (a) ZnO films, (b) ZnO-based micro/nanoferns, and (c) ZnO-based nanoparticles.

Tauc plots of the ZnO-based photocatalysts

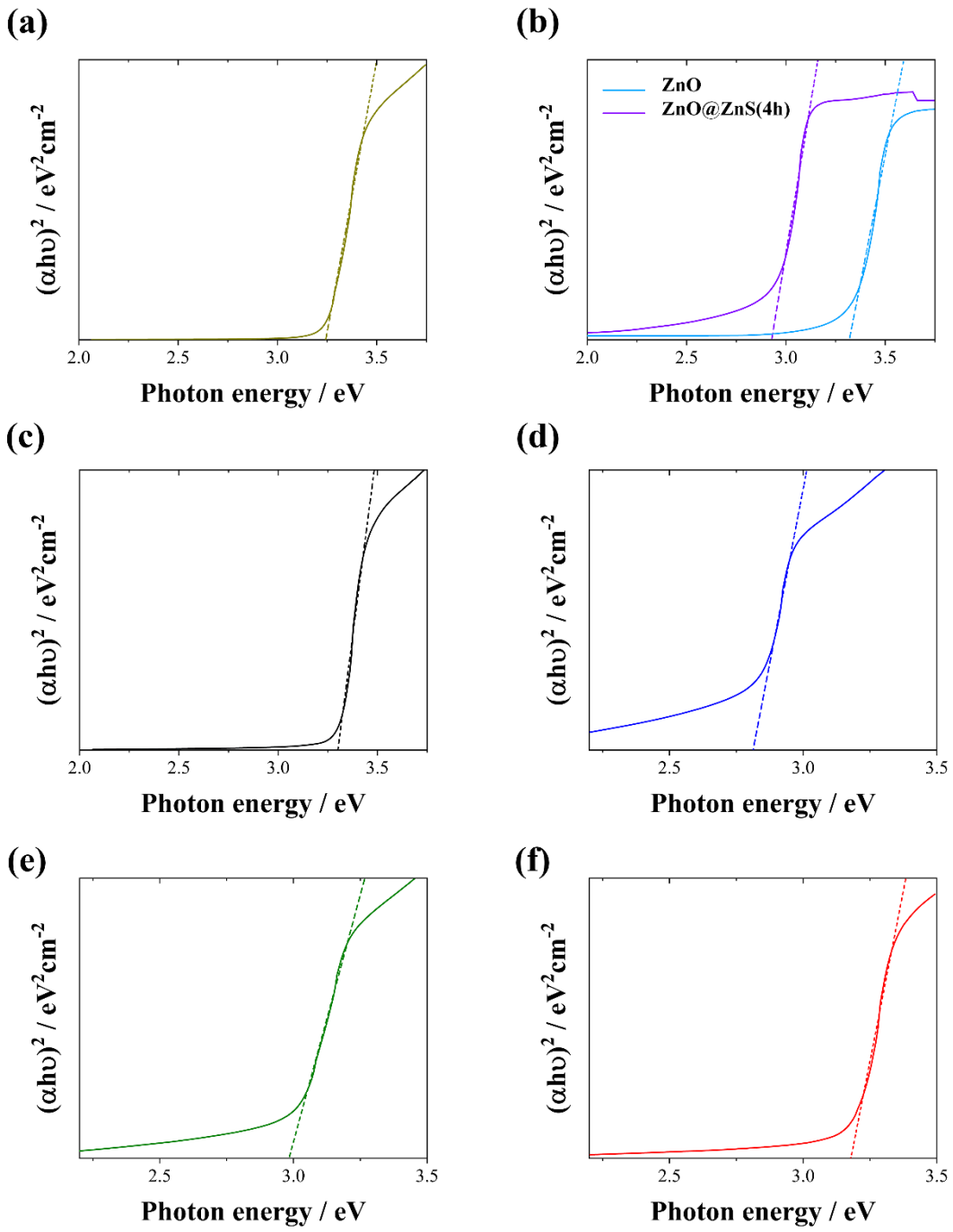

Figure S6: Tauc plots from the UV-vis analysis of (a) ZnO films, (b) ZnO-based nanoparticles, (c) the ZnO nano/microferns, (d) the ZnO@ZnS(4h) nano/microferns, (e) the ZnO@ZnS(8h) nano/microferns, and (f) the ZnO@ZnS(12h) nano/microferns.

Photoluminescence spectra of ZnO-based photocatalysts

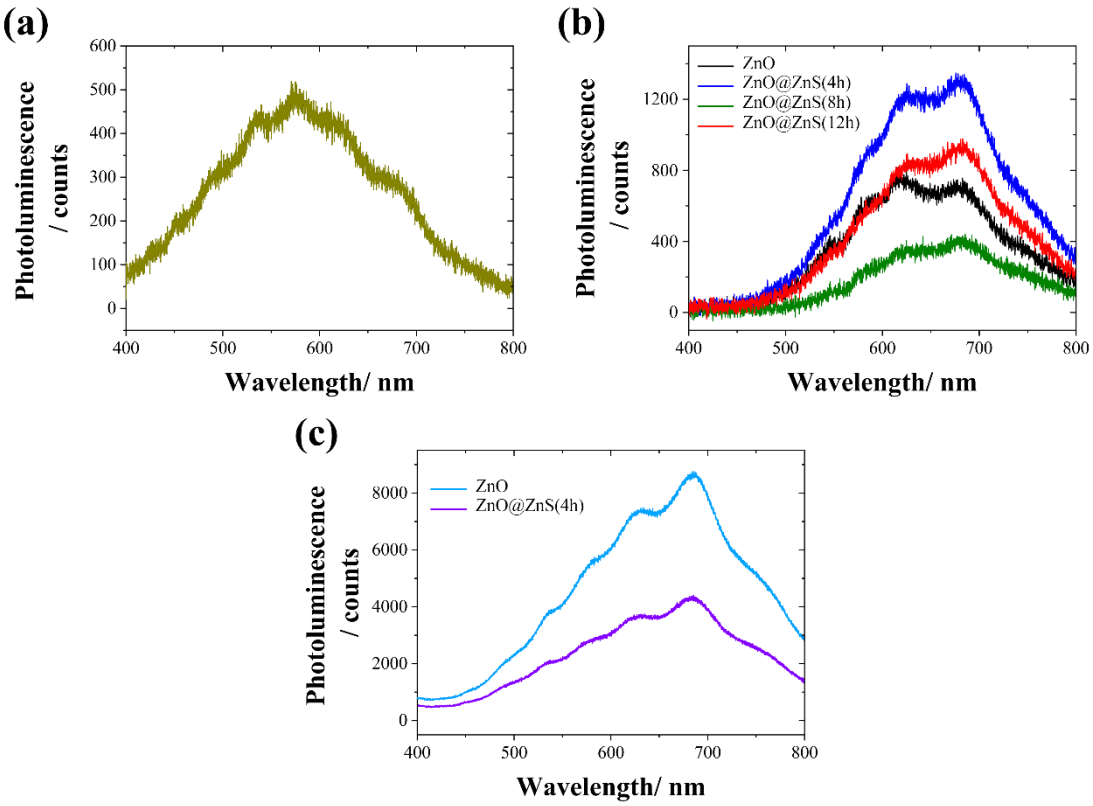

Figure S7: Room temperature photoluminescence spectra of (a) the ZnO films, (b) the ZnO-based micro/nanoferns, (c) the ZnO-based nanoparticles.

Hydroxyl radical trapping experiments

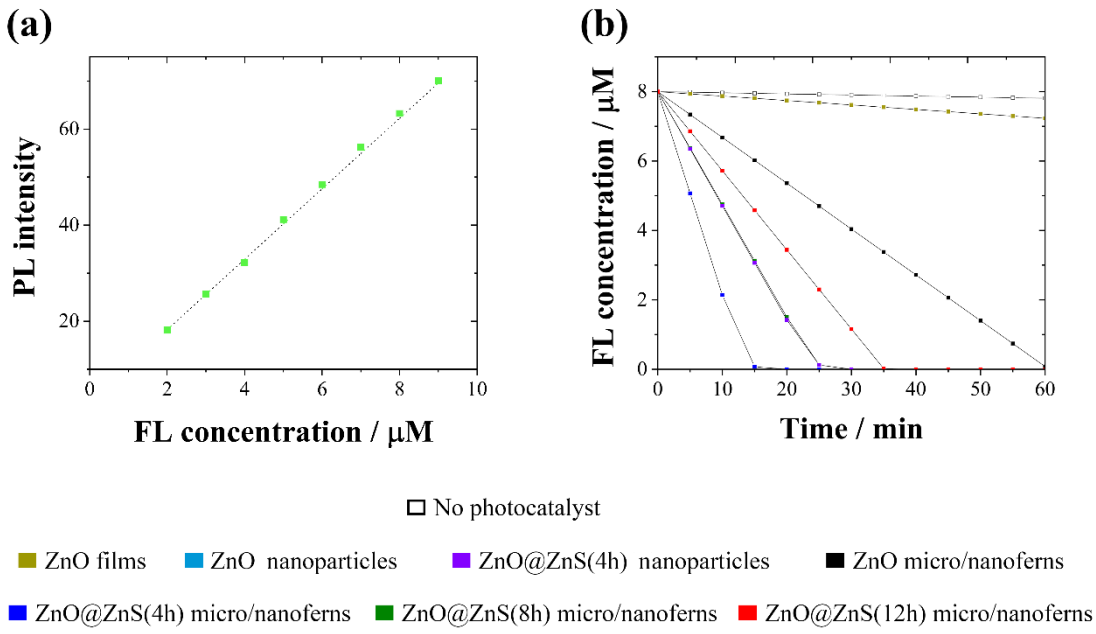

Figure S8: (a) Calibration of Fluorescein sodium in aqueous solution using the PL intensity at 515 nm (λ_{ex} = 303). (b) Time-dependent evolution of the Fluorescein sodium concentration under UV-filtered simulated sunlight in the absence and using 400 mg L^{-1} of ZnO-based photocatalysts (temperature = 30.0 ±0.1 ºC).

Mineralization efficiencies of ZnO-based photocatalysts

The performance of each photocatalyst to degrade the multi-pollutant solution was evaluated by quantifying the reduction in TOC (**Figure S9**) after the irradiation of each sample under natural sunlight during 210 min. As **Tables 1 and S1** show, the ZnO@ZnS(4h) core@shell micro/nanoferns were the most efficient photocatalyst. Such differences in the photocatalytic performance can be explained by the combination of three synergetic elements: (i) the electronic properties, which determine the ability of the photocatalysts to produce reactive oxygen spices (ROS) when irradiated with visible light, and (ii) the shape and architecture, which strongly determine not only the affinity and surface reactivity of the photocatalysts, but also their light trapping ability. In that sense, large surface areas, abundant active sites, and an enhanced ability to trap light and pollutants of the ZnO micro/nanoferns due to their dendritical architecture were responsible for the improved activity of micro/nanoferns compared with that of ZnO films and ZnO nanoparticles. By extension, the increased photocatalytic degradation and mineralization efficiencies of the ZnO@ZnS core@shell nanoparticles and micro/nanoferns compared to those of pristine ZnO architectures resulted from their narrower bandgap and, in turn, from their exceptional ability to harvest larger fractions of visible light. Among the various studied photocatalysts, ZnO@ZnS(4h) core@shell micro/nanoferns are the best candidates for photodecontamination in terms of mineralization efficiency, since they combine a narrower bandgap and a dendritical microstructure. A longer sulfidation did not improve the electronic properties, and the microfern architecture was affected by a reduction in the active and accessible surface area, which in conjunction reduced the catalytic performance.

Table S1: Photocatalytic degradation efficiency of MB (5 ppm) + 4-NP (5 ppm) + Rh-B (5 ppm) polluted solutions under artificial sunlight (λ> 400 nm), and natural sunlight (λ> 400 nm), by using the ZnO film, the ZnO and ZnO@ZnS core@shell nanoparticles and the ZnO and ZnO@ZnS core@shell bioinspired fern-shape microleaves (0.4 mg mL^{-1}).

Photocatalyst	TOC of pollutant solution without irradiation / ppm	Artificial UV-filtered sunlight irradiation (210 min λ> 400 nm) Mineralization efficiency / %	Natural UV-filtered sunlight irradiation (210 min λ> 400 nm) Mineralization efficiency / %
ZnO film	15.14 ± 0.02	5.1 ± 0.7	4.3 ± 0.5
ZnO nanoparticles	15.26 ± 0.13	19.2 ± 0.4	17.9 ± 0.1
ZnO@ZnS(4h) nanoparticles	15.19 ± 0.09	68.4 ± 0.2	61.7 ± 0.9
ZnO micro/nanoferns	15.18 ± 0.07	24.1 ± 0.3	20.1 ± 0.4
ZnO@ZnS(4h) micro/nanoferns	15.34 ± 0.11	86.9 ± 0.8	81.4 ± 0.3
ZnO@ZnS(8h) micro/nanoferns	15.05 ± 0.09	76.5 ± 1.2	71.0 ± 0.6
ZnO@ZnS(12h) micro/nanoferns	15.44 ± 0.12	45.9 ± 0.9	39.9 ± 0.9

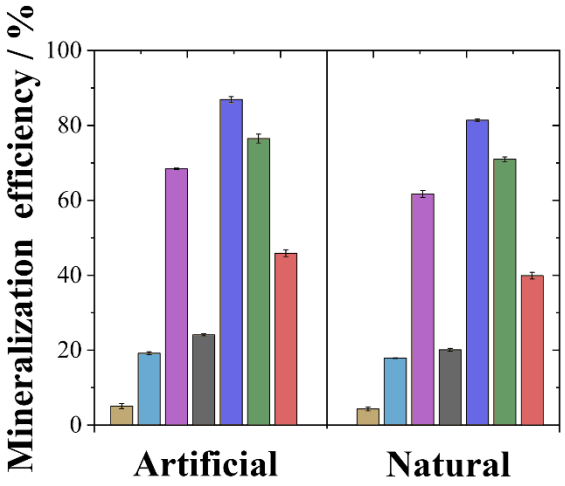

Figure S9: Mineralization efficiency after 210 min of artificial and natural (λ > 400 nm) sunlight irradiation for the ZnO film (dark golden), the ZnO nanoparticles (dark cyan), the ZnO@ZnS(4h) nanoparticles (dark violet), the ZnO micro/nanoferns (gray), ZnO@ZnS(4h) micro/nanoferns (blue), the ZnO@ZnS(8h) micro/nanoferns (green), and the ZnO@ZnS(12h) micro/nanoferns (red).

FE-SEM micrographs of reused micro/nanofern photocatalysts

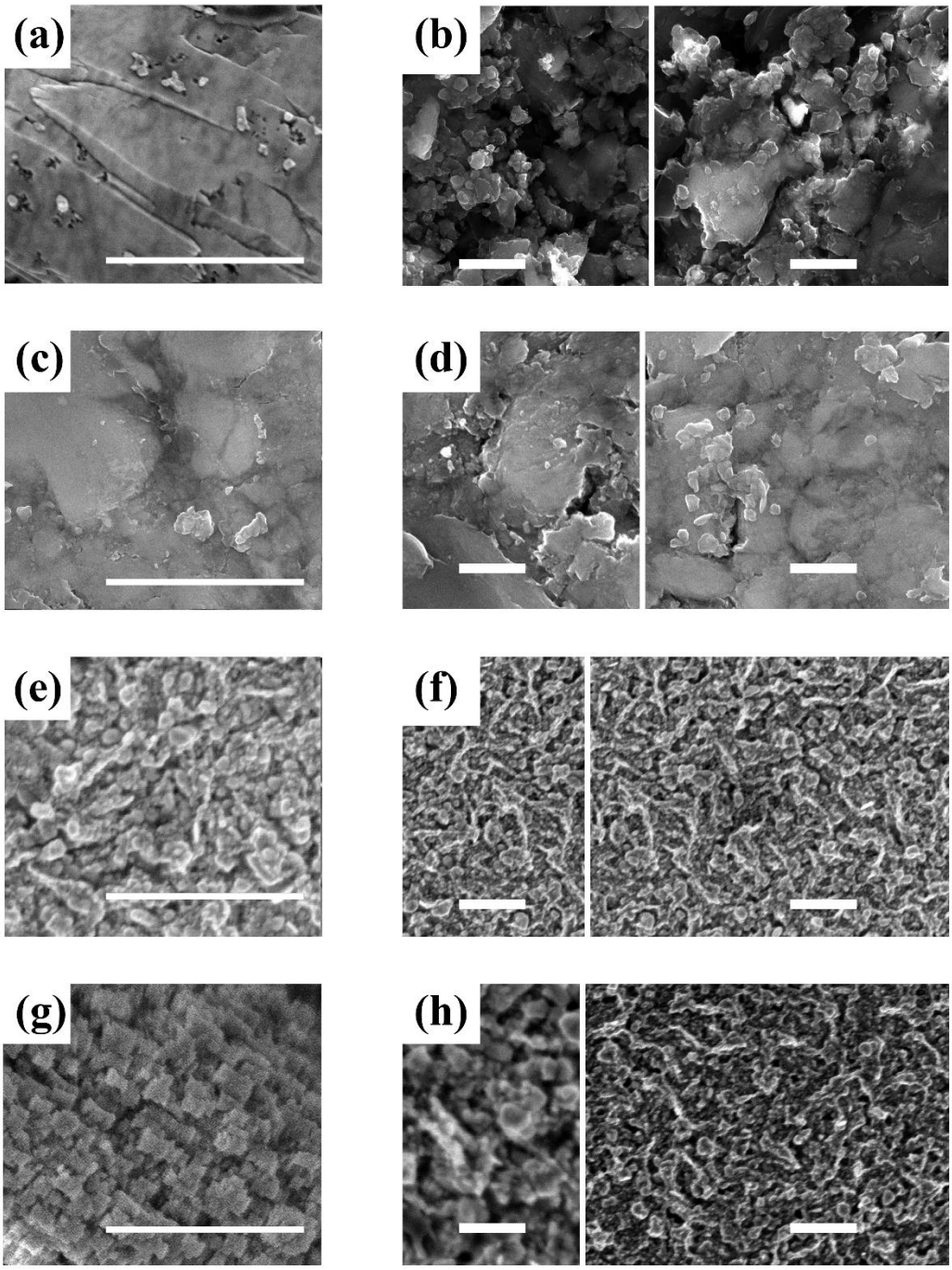

Figure S10: FE-SEM micrographs of fern-like bioinspired microleaves of (a, b) ZnO, (c, d) ZnO@ZnS(4h), (e, f) ZnO@ZnS(8h), and (g, h) ZnO@ZnS(12h) after their continuous irradiation in fresh water during (a, c, e , and g) 0 and (b, d , f, and h) 96 h under artificial sunlight (λ>400 nm). Scale bar: 500 nm (a, c), 350 (e, g) or 90 nm (b, d, f, and h).

Spirulina (Arthrospira) platensis tank

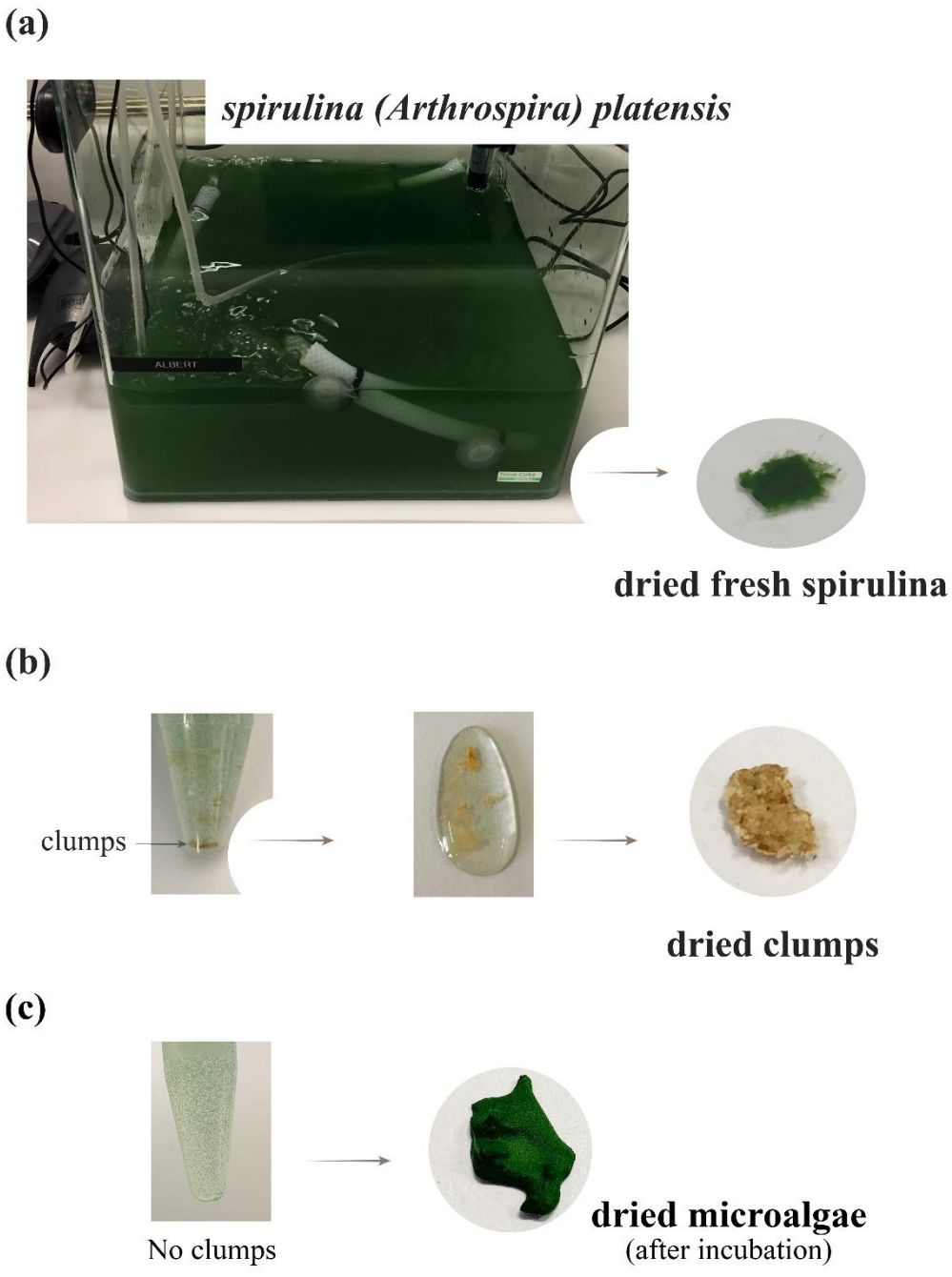

Figure S11: (a) *Spirulina (Arthrospira) platensis* tank. (b) Dried clumps which appeared after the incubation of 400 mg L^{-1} of ZnO nanoparticles with microalgae during 96 h. (c) Dried microalgae after the incubation of 400 mg L^{-1} of ZnO@ZnS(4h) micro/nanoferns with microalgae during 96 h.

Ecotoxicological effect of ZnO and ZnO@ZnS(4h) nanoparticles on microalgae

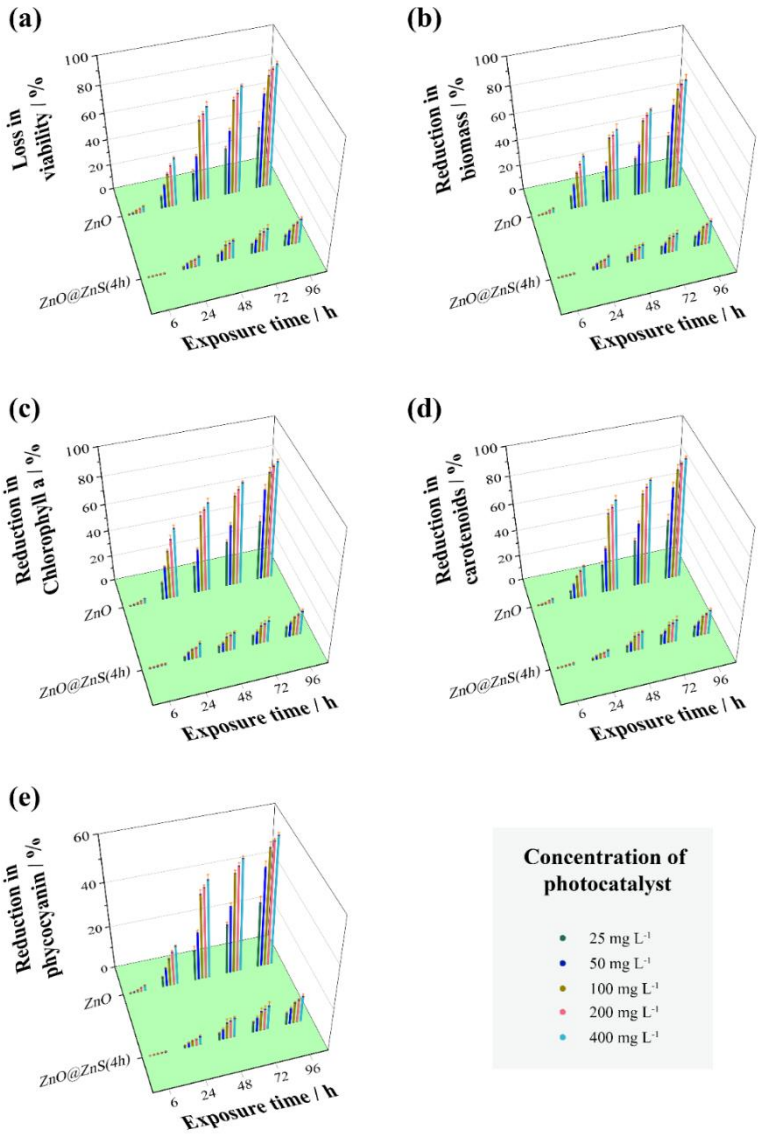

Figure S12: Percentage of loss in (a) microalgae viability, (b) microalgae biomass, (c) chlorophyll-a of microalgae, (d) carotenoids of microalgae, and (e) phycocyanin pigment of microalgae for the treatment with 25, 50, 100, 200, and 400 mg L^{-1} of ZnO and ZnO@ZnS(4h) nanoparticles, after exposure times of 6, 24, 48, 72, and 96 h. The microalgae cultures were irradiated 8 h per day with continuous UV-filtered simulated sunlight (light intensity of 740 ± 15 lx), starting the first irradiation cycle when photocatalysts were introduced in microalgae culture. Percentages are relative to the control (microalgae culture without catalyst) cultivated in the same experimental conditions.

Percentage of photosynthetic pigments of *Spirulina* microalgae treated with ZnO-based biomimetic microferns

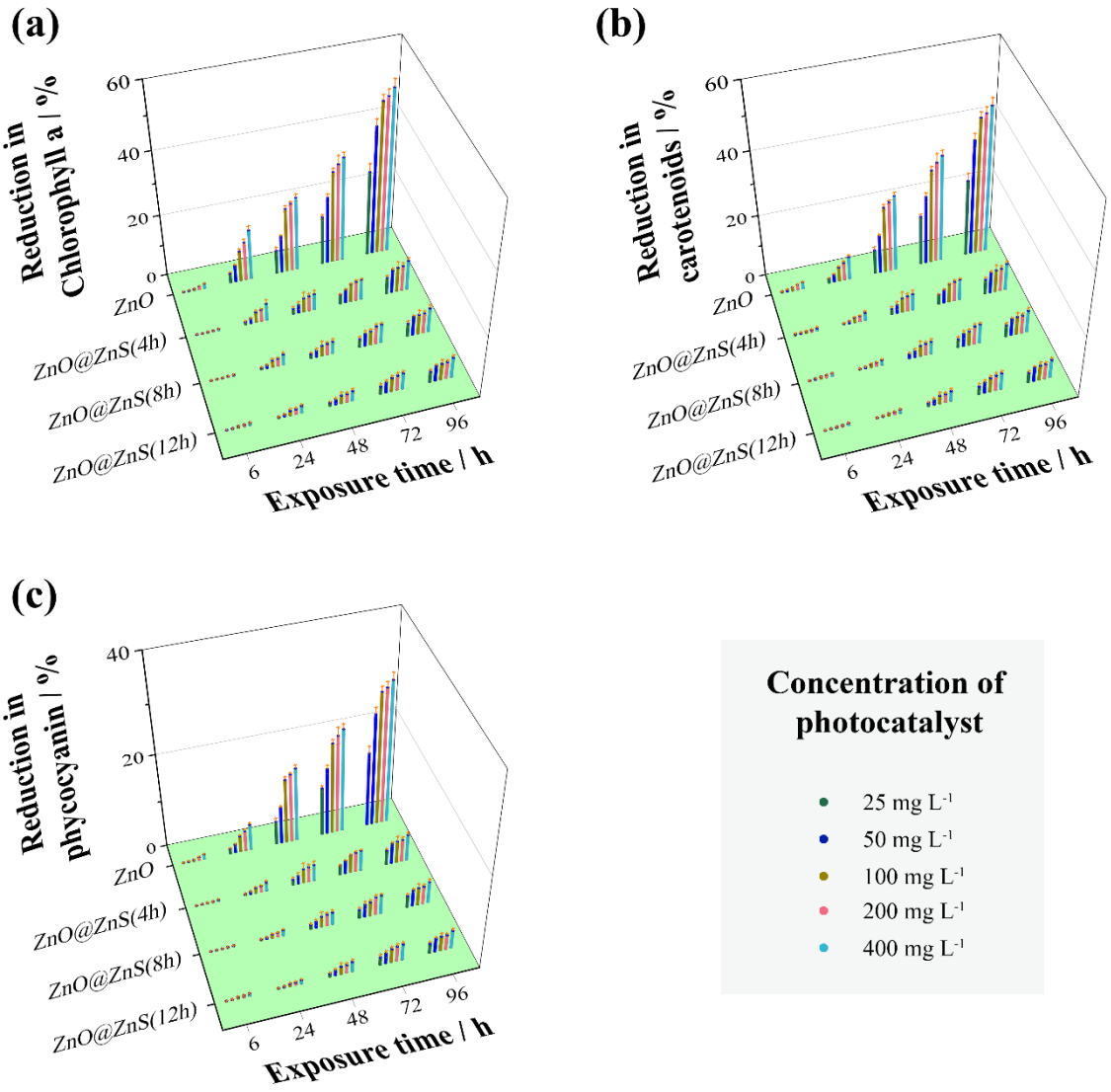

Figure S13: Percentage of loss in (a) chlorophyll-a of the microalgae, (b) carotenoids of the microalgae, and (c) phycocyanin pigment of the microalgae for the treatment with 25, 50, 100, 200, and 400 mg L^{-1} of ZnO-based bioinspired micro/nanoferns after exposure times of 6, 24, 48, 72, and 96 h. The microalgae cultures were irradiated 8 h per day with continuous simulated sunlight (light intensity of 740 ± 15 lx), starting the first irradiation cycle when photocatalysts were introduced in microalgae culture. Percentages are relative to the control (microalgae culture without catalyst) cultivated in the same experimental conditions.

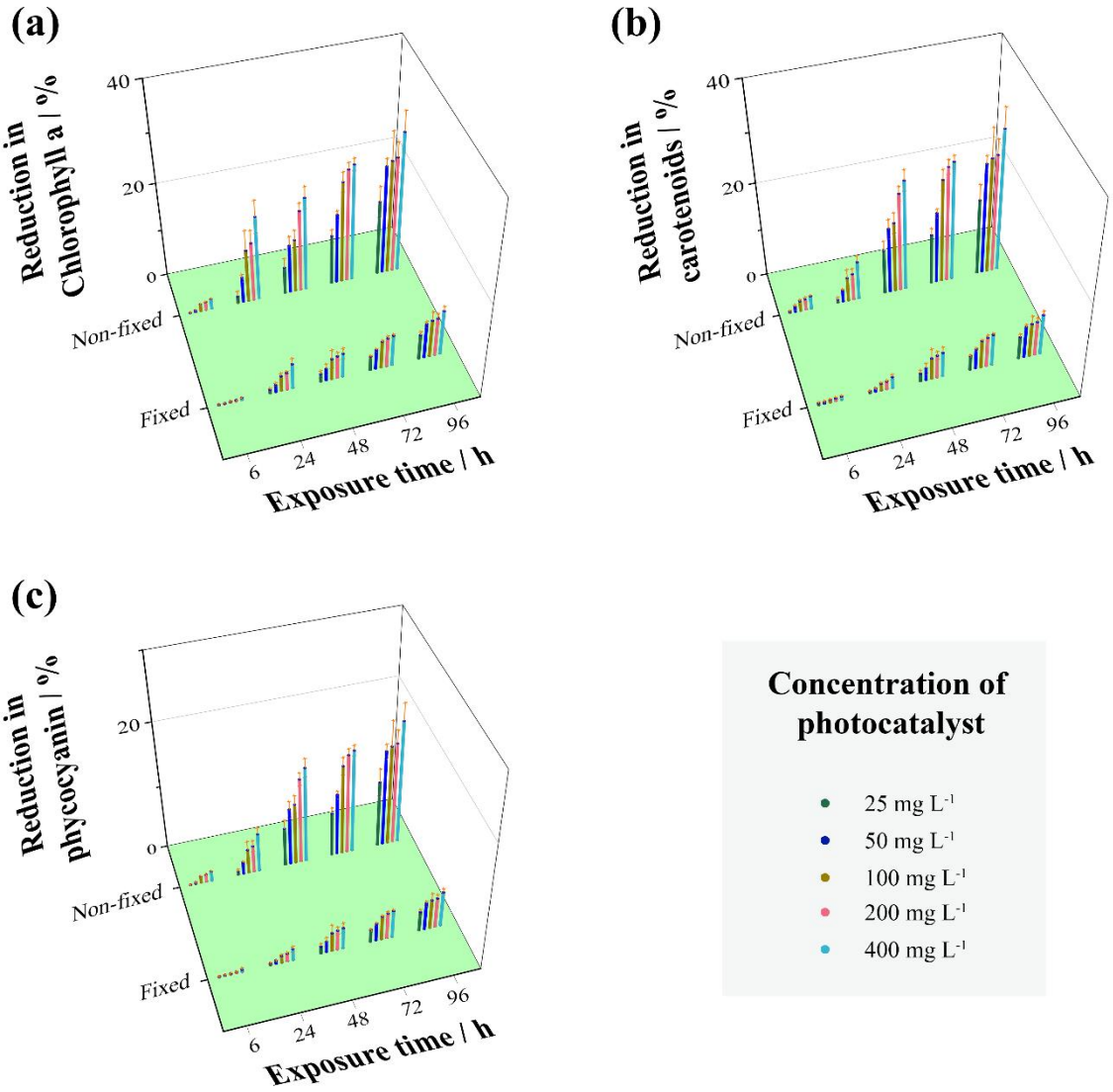

Figure S14: Percentage of loss in (a) chlorophyll-a of the microalgae, (b) carotenoids of the microalgae, and (c) phycocyanin pigment of the microalgae for the treatment with 25, 50, 100, 200, and 400 mg L^{-1} of fixed and non-fixed ZnO@ZnS(4h) micro/nanoferns after an exposure time of 6, 24, 48, 72, and 96 h. The microalgae cultures were irradiated 8 h per day with continuous simulated sunlight (light intensity of 740 ± 15 lx), starting the first irradiation cycle when photocatalysts were introduced in microalgae culture. Percentages are relative to the control (microalgae culture without catalyst) cultivated in the same experimental conditions.